

1 Diurnal variations in oxygen and nitrogen isotopes of atmospheric 2 nitrogen dioxide and nitrate: implications for tracing NO_x oxidation 3 pathways and emission sources

4 Sarah Albertin^{1,2}, Joël Savarino², Slimane Bekki¹, Albane Barbero², Roberto Grilli², Quentin Fournier³,
5 Irène Ventrillard³, Nicolas Caillon², Kathy Law¹

6 ¹LATMOS/IPSL, Sorbonne Université, UVSQ, CNRS, 75005 Paris, France.

7 ²IGE, Univ. Grenoble Alpes, CNRS, IRD, Grenoble INP, 38000 Grenoble, France.

8 ³LIPhy, Univ. Grenoble Alpes, CNRS, 38000 Grenoble, France.

9 *Correspondence to:* Sarah Albertin (sarah.albertin@univ-grenoble-alpes.fr)

10 **Abstract.** The oxygen ($\Delta^{17}\text{O}$) and nitrogen ($\delta^{15}\text{N}$) isotopic compositions of atmospheric nitrate (NO_3^-) are widely used as
11 tracers of its formation pathways, precursor (nitrogen oxides (NO_x) \equiv nitric oxide (NO) + nitrogen dioxide (NO_2)) emission
12 sources, and physico-chemical processing. However, the lack of observations on the multi-isotopic composition of NO_2
13 maintains significant uncertainties regarding the quantitative links between the isotopic composition of NO_x and NO_3^- ,
14 which ultimately may bias inferences on NO_3^- formation processes and distribution of sources, particularly in winter urban
15 atmospheres. We report here on the first simultaneous atmospheric observations of $\Delta^{17}\text{O}$ and $\delta^{15}\text{N}$ in NO_2 ($n = 16$) and NO_3^-
16 ($n = 14$). The measurements were carried out at sub-daily (~ 3 h) resolution over two non-consecutive days in an Alpine city
17 in February 2021. A strong diurnal signal is observed in both NO_2 and NO_3^- multi-isotopic composition. $\Delta^{17}\text{O}$ of NO_2 and
18 NO_3^- ranges from 19.6 ‰ to 40.8 ‰ and from 18.3 ‰ to 28.1 ‰, respectively. During the day and night, the variability of
19 $\Delta^{17}\text{O}(\text{NO}_2)$ is mainly driven by the oxidation of NO by ozone, with a substantial contribution from peroxy radicals in the
20 morning. NO_3^- mass balance equations, constrained by observed $\Delta^{17}\text{O}(\text{NO}_2)$, suggest that during the first day of sampling,
21 most of NO_3^- was formed locally from the oxidation of NO_2 by hydroxyl radicals by day, and via heterogeneous hydrolysis
22 of dinitrogen pentoxide at night. For the second day, calculated and observed $\Delta^{17}\text{O}(\text{NO}_3^-)$ do not match, particularly daytime
23 values; the possible effects on $\Delta^{17}\text{O}(\text{NO}_3^-)$ of a Saharan dust event that occurred during this sampling period and of winter
24 boundary layer dynamics are discussed. $\delta^{15}\text{N}$ of NO_2 and NO_3^- ranges from -10.0 ‰ to 19.7 ‰ and from -4.2 ‰ to 14.9 ‰,
25 respectively. Consistent with theoretical predictions of N isotope fractionation, the observed variability of $\delta^{15}\text{N}(\text{NO}_2)$ is
26 explained by significant post-emission equilibrium N fractionation. After accounting for this effect, vehicle exhaust is found
27 to be the primary source of NO_x emissions at the sampling site. $\delta^{15}\text{N}(\text{NO}_3^-)$ is closely linked to $\delta^{15}\text{N}(\text{NO}_2)$ variability,
28 bringing further support to relatively fast and local NO_x processing. Uncertainties on current N fractionation factors during
29 NO_2 to NO_3^- conversion are underlined. Overall, this detailed investigation highlights the potential and necessity to use

30 simultaneously $\Delta^{17}\text{O}$ and $\delta^{15}\text{N}$ in NO_2 and NO_3^- in order to better constrain quantitative inferences on the sources and
31 formation chemistry of NO_3^- in urban environments in winter.

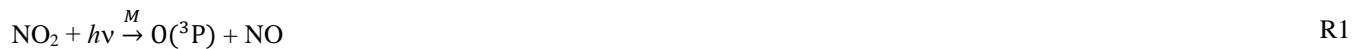
32 **1 Introduction**

33 Despite extensive efforts in emission controls in recent decades, global anthropogenic emissions of nitrogen oxides ($\text{NO}_x \equiv$
34 nitrogen monoxide (NO) + nitrogen dioxide (NO_2)) remain more than two orders of magnitude higher than before the
35 Industrial Revolution (Hoesly et al., 2018). Atmospheric nitrate ($\text{NO}_3^- \equiv$ nitric acid (HNO_3) + particulate nitrate ($p\text{-NO}_3^-$)), is
36 the main end-product of NO_x oxidation and a key component of fine particulate matter (PM), which adversely affects human
37 health (WHO, 2021) and contributes to climate change (Masson-Delmotte et al., 2021). NO_3^- can be transported far from
38 emission sources and can be removed from the atmosphere through dry and wet deposition within hours to days (Alexander
39 et al., 2020; Park et al., 2004). The additional input of this "reactive" nitrogen (N_r) into natural environments is known to
40 have detrimental consequences, particularly regarding biodiversity and water quality (Galloway et al., 2008; Vitousek et al.,
41 1997). It is therefore important to have a comprehensive understanding of NO_x emission sources and oxidation processes, on
42 which effective air quality and climate change mitigation strategies rely (e.g., Bauer et al., 2007; Huang et al., 2014; Shah et
43 al., 2018; Tsimpidi et al., 2008; Wang et al., 2013, 2020).

44
45 Several studies noted that the response of NO_3^- concentration in air to NO_x emission reduction is contrasted,
46 particularly in winter (e.g., Shah et al., 2018; Tørseth et al., 2012; Wang et al., 2020; Zhou et al., 2019). This is because a
47 variety of factors controls the NO_x conversion efficiency and the NO_3^- content in PM, including precursor emission sources,
48 complex multiphase chemical reactions with other reactive species, and environmental conditions (e.g., temperature, relative
49 humidity, solar radiation) (Zhang et al., 2015). It remain difficult to assess the contribution of each parameter to the non-
50 linear N_r chemistry, which is partly driven by close links between changes in aerosol acidity, gas-particle partitioning, and
51 atmospheric oxidation capacity (Shah et al., 2018; Fu et al., 2020; Shi et al., 2019; Li et al., 2021b). Ozone (O_3) and
52 hydroxyl radicals (OH) (Finlayson-Pitts and Pitts, 2000), are the major oxidants in the atmosphere whose chemical cycles
53 are largely controlled by solar radiation. As a result, there are significant diurnal and seasonal variations in NO_x chemistry
54 (e.g., Prabhakar et al., 2017; Alexander et al., 2020). Notably, NO_3^- formation is generally dominated by homogeneous OH
55 oxidation and heterogeneous O_3 chemistry during day/summer and night/winter, respectively (Alexander et al., 2020).
56 However, assessing the relative contributions of individual formation channels, together with their sensitivity to
57 environmental parameters, is not straightforward and requires extensive in situ observations combined with modelling tools
58 (e.g., Alexander et al., 2020; Brown, 2006; Newsome and Evans, 2017; Xue, 2022; Prabhakar et al., 2017).

59

60 Upon release into the atmosphere, NO_x, mainly emitted as NO, undergoes oxidation to form NO₂. During the day, a
61 rapid photochemical equilibrium is established between NO and NO₂, known as the "photostationary state" (PSS; Leighton,
62 1961), via key interconversion reactions (Reactions R1–R3):



63 This cycle can be disturbed by peroxy radicals (RO₂ ≡ hydroperoxyl radical (HO₂) + methyl peroxy radical (CH₃O₂)) via
64 typically Reaction (R4):



65 Note that in polluted atmospheres where NO_x mixing ratios often exceed ppb levels, Reaction (R4) followed by Reactions
66 (R1)–(R2) lead to the formation of O₃ (Crutzen, 1979). Although the role of RO₂ in NO_x oxidation is crucial in O₃ formation
67 and NO_x oxidation rate, measuring RO₂ mixing ratio remains challenging due to the need for state-of-the art instrumentation
68 coupled with photochemical models to establish chemical budgets (e.g., Ren et al., 2006; Tan et al., 2018). While NO is
69 usually oxidised relatively quickly into NO₂ in summer due to the high levels of O₃ and solar radiation, the shorter day
70 length and lower temperature in winter result in a contrasted NO_x cycling. In particular, the formation of a temperature
71 inversion at the surface can trap pollutants emitted close to the surface in a shallow layer for hours to days (e.g., Largeron
72 and Staquet, 2016; Olofson et al., 2009). Under those conditions, it is not uncommon for O₃ levels to be very low due to
73 quasi-complete titration by NO, which can have further impacts on the atmospheric oxidation capacity. However,
74 pronounced O₃ pollution episodes may also arise in winter in highly polluted areas, such as in oil-producing regions due to
75 intense VOCs emissions (Edwards et al., 2014) or in China, where pollution control strategies mainly target NO_x while
76 VOCs emissions remain more or less constant (Ren et al., 2022). In urban areas, NO₂ is generally mainly removed from the
77 atmosphere by reaction with OH during the day via Reaction (R5) (Dentener and Crutzen, 1993):



78 NO₂ can also react with O₃ to form nitrate radicals (NO₃) via Reaction (R6):



79 However, NO₃ is rapidly photolyzed during the day regenerating back NO₂ (Wayne et al., 1991). Another important NO₃
80 loss reaction is that with NO in polluted environments (Brown and Stutz, 2012). At night, without photolytic activity and

81 lower precursor emissions, the lifetime of NO₃ radicals substantially increases. NO₃ reacts with NO₂ to form dinitrogen
82 pentoxide (N₂O₅; Reaction R7), which then undergoes heterogeneous hydrolysis to form HNO₃ (Reaction R8):



83 Reaction (R7) is temperature dependent, so N₂O₅ can eventually decompose to reform NO₂ and NO₃, with the N₂O₅/NO₃
84 ratio being negatively correlated with temperature. N₂O₅ is an important nocturnal sink for NO_x, notably in winter in urban
85 atmospheres due to high aerosol loads and low temperatures. However, the efficiency of Reaction (R8) is difficult to
86 determine because it strongly depends on parameters such as the aerosol surface density and its chemical composition
87 (Brown, 2006), which are not often well characterised. In addition, NO₃ can react with hydrocarbons to produce HNO₃,
88 which could significantly contribute to the formation of NO₃⁻ in industrialised regions with high hydrocarbon emissions
89 (Brown et al., 2011). It is estimated that the Reactions (R1) to (R8) lead to the formation of 82 % of NO₃⁻ near the surface on
90 a global scale (Alexander et al., 2020). In polluted environments, the respective contributions of Reaction (R5) (OH
91 pathway) and Reactions (R6)–(R8) (N₂O₅ pathway) are more contrasted and are still debated (e.g., Chan et al., 2021; Fu et
92 al., 2020). In addition, the reaction of N₂O₅ with chlorine on aerosols can contribute to NO₃⁻ production in urban
93 atmospheres (Thornton et al., 2010), with further impacts on O₃ production in continental polluted atmosphere in winter
94 (Wang et al., 2019a). Other reactions, such as those involving halogen and organic intermediates, may become significant for
95 NO₃⁻ production in specific regions, such as in polar, oceanic, and coastal areas (Alexander et al., 2020; Penkett et al., 2007;
96 Savarino et al., 2013; Simpson et al., 2015).

97

98 To help better constrain the atmospheric N_r chemistry and budget, the last three decades have seen a growing interest in
99 stable oxygen (O) and nitrogen (N) isotopes, notably in NO₃⁻ (Elliott et al., 2019; Savard et al., 2018). The isotopic
100 composition is reported as an isotopic enrichment (δ) with respect to a reference material, defined as $\delta = (R_{\text{sample}}/$
101 $R_{\text{reference}} - 1)$, and expressed in per mill (‰). *R* refers to the elemental abundance ratio of the heavy isotope to the light
102 isotope (e.g., ¹⁸O/¹⁶O; ¹⁷O/¹⁶O; ¹⁵N/¹⁴N) in the sample, and in an international isotopic reference material (Vienna Standard
103 Mean Ocean Water for O; Li et al., 1988), and atmospheric N₂ for N; Mariotti, 1984). A powerful tool to help trace the
104 relative importance of different NO_x to NO₃⁻ oxidation pathways is through the use of the ¹⁷O-excess ($\Delta^{17}\text{O} = \delta^{17}\text{O} - 0.52 \times$
105 $\delta^{18}\text{O}$). $\Delta^{17}\text{O}$ is transferred to NO₃⁻ by O₃ which possesses a very unique $\Delta^{17}\text{O}$ ((26.2 ± 1.3) ‰; Vicars and Savarino, 2014)
106 due to mass-independent fractionation during its formation process (Thiemens, 2006). In comparison, the $\Delta^{17}\text{O}$ of other
107 atmospheric oxidants such as OH is near zero due to isotopic exchange with atmospheric water vapor (Dubey et al., 1997).
108 Similarly, as the isotopic anomaly of atmospheric O₂ is very close to 0 ‰ (Barkan and Luz, 2003), and since RO₂ are mostly
109 produced by the reactions R + O₂ and H + O₂, $\Delta^{17}\text{O}$ of RO₂ can be considered negligible (Alexander et al., 2020). Therefore,

110 $\Delta^{17}\text{O}$ in NO_3^- represents a unique tracer of the O_3 implication in its formation processes, that can provide valuable
111 constraints on the relative contributions of individual reactions (e.g., Morin et al. 2011, Alexander et al., 2009; Michalski et
112 al., 2003). By a simple mass balance calculation of O atoms in NO_3^- , the ^{17}O -excess of NO_3^- produced by an individual NO_2
113 to NO_3^- conversion process i ($\Delta^{17}\text{O}(\text{NO}_3^-)_i$) can be expressed as:

$$\Delta^{17}\text{O}(\text{NO}_3^-)_i = \frac{2}{3} \times \Delta^{17}\text{O}(\text{NO}_2) + \frac{1}{3} \times \Delta^{17}\text{O}(\text{add. O})_i \quad (1)$$

114 where $\Delta^{17}\text{O}(\text{NO}_2)$ is the ^{17}O -excess of atmospheric NO_2 and $\Delta^{17}\text{O}(\text{add. O})_i$ is the transferrable ^{17}O -excess of the oxidant
115 responsible for the conversion of NO_2 in NO_3^- (Michalski et al., 2003). From Eq. (1), if $\Delta^{17}\text{O}(\text{NO}_2)$ is constrained, one can
116 derive individual $\Delta^{17}\text{O}$ transfer to NO_3^- relative to a i conversion process and compare this value with observed $\Delta^{17}\text{O}(\text{NO}_3^-)$.
117

118 Recent studies in urban areas have attempted to interpret the variability of $\Delta^{17}\text{O}(\text{NO}_3^-)$ in aerosols in order to quantify
119 the relative contribution of homogeneous and heterogeneous processes to NO_3^- formation (e.g., Fan et al., 2023, 2022; He et
120 al., 2020, 2018; Lim et al., 2022; Wang et al., 2023, 2019b; Kim et al., 2023; Zhang et al., 2022b; Li et al., 2022b). However,
121 to that end, it is necessary to have a clear quantitative understanding of the transfers of $\Delta^{17}\text{O}$ in the N_r cycle. To date, due to
122 very limited observational data, there is a lack of well-established knowledge on the dynamics of $\Delta^{17}\text{O}$ in NO_2 , the key
123 intermediate species in the formation of NO_3^- . Consequently, strong assumptions about $\Delta^{17}\text{O}(\text{NO}_2)$ have to be made when
124 interpreting $\Delta^{17}\text{O}(\text{NO}_3^-)$ measurements, which could potentially lead to biased conclusions. Notably, the most difficult
125 regions for the interpretation of NO_3^- records are potentially polluted areas where the isotopic composition of NO_2 is
126 expected to be highly variable in space and time. Most studies typically estimate $\Delta^{17}\text{O}(\text{NO}_2)$ during the day by assuming that
127 an isotopic steady state (ISS) is reached between NO_x and O_3 resulting in $\Delta^{17}\text{O}(\text{NO}_2)$ depending only on the relative
128 contributions of different oxidants to NO oxidation. A recent study reported the first in situ observations of $\Delta^{17}\text{O}(\text{NO}_2)$ in an
129 urban environment (Grenoble, France) in spring (Albertin et al., 2021). Time resolved NO_2 sampling (ca. 3 h) during 24 h
130 revealed a strong diurnal cycle in $\Delta^{17}\text{O}(\text{NO}_2)$, reaching ca. 40 ‰ during the day and decreasing down to ca. 20 ‰ at night.
131 The observed $\Delta^{17}\text{O}(\text{NO}_2)$ values and diurnal variability were consistent with its expected behaviour derived from $\Delta^{17}\text{O}$ mass
132 balance equations under the ISS assumption during the day. However, this first $\Delta^{17}\text{O}(\text{NO}_2)$ dataset is very short. More
133 measurements are needed to test in different environments and seasons the applicability of this new isotopic tool and to assess
134 whether the ISS is still valid. At night, the low $\Delta^{17}\text{O}(\text{NO}_2)$ measured by Albertin et al. (2021) is consistent with the oxidation
135 of freshly emitted NO by O_3 . Nonetheless, since the timescale for the oxidation of NO_2 into NO_3^- is thought to exceed the
136 duration of the night (Alexander et al., 2020), it is also common to assume that the isotopic composition of nocturnal NO_2
137 reflects more daytime formation and conditions of the previous days. While this assumption may hold true in remote areas
138 (Morin et al., 2011), significant uncertainties subsist in urban areas where the nighttime NO_3^- chemistry may be more

139 efficient. In such circumstances, the production of NO_3^- from NO_2 formed at night would lead to a lower than expected $\Delta^{17}\text{O}$
140 transfer to NO_3^- . For these reasons, the dual survey of the O isotopic composition of NO_2 and NO_3^- would certainly help to
141 accurately interpret $\Delta^{17}\text{O}(\text{NO}_3^-)$ observations in polluted atmospheres, particularly with sampling at sub-daily time scales
142 which would allow to study the diurnal dynamics of $\Delta^{17}\text{O}(\text{NO}_2)$ and its links with $\Delta^{17}\text{O}(\text{NO}_3^-)$.

143
144 In addition to $\Delta^{17}\text{O}$, $\delta^{15}\text{N}$ in NO_3^- ($\delta^{15}\text{N}(\text{NO}_3^-)$) can be used as a tracer of NO_3^- sources and/or chemical processing. As
145 different NO_x emission sources have often distinct $\delta^{15}\text{N}$ -fingerprints depending on the NO_x production mechanism (Heaton,
146 1990; Felix et al., 2012; Fibiger and Hastings, 2016; Walters et al., 2015a, b; Yu and Elliott, 2017; Miller et al., 2018),
147 $\delta^{15}\text{N}(\text{NO}_3^-)$ is a potentially valuable tool to trace the origins of its gaseous precursor. However, due to N fractionation effects
148 associated with physico-chemical processing, $\delta^{15}\text{N}$ is altered during the conversion of NO_x to NO_3^- (Elliott et al., 2019).
149 Therefore, the variability of $\delta^{15}\text{N}(\text{NO}_3^-)$ can be attributed to: (1) a change in NO_x emission sources and (2) N isotopic
150 fractionations between NO and NO_2 , between NO_2 and NO_3^- , and during the transport of NO_3^- . These effects co-exist with
151 relative contributions varying according to environmental conditions and the mix of NO_x emissions. Numerous observations
152 in diverse environments have emphasised the substantial influence of N fractionation effects in altering the original ^{15}N
153 composition of emitted gaseous NO_3^- precursors (e.g., (Bekker et al., 2023; Chang et al., 2018; Geng et al., 2014; Luo et al.,
154 2023; Vicars et al., 2013; Li et al., 2021a). Although some N fractionation factors are available from calculations (Walters
155 and Michalski, 2015) and laboratory experiments (Li et al., 2020; Walters et al., 2016), there is still a lack of observational
156 constraints on the magnitude of the N isotopic partitioning between NO_x and NO_3^- , which could lead to biased
157 interpretations of $\delta^{15}\text{N}(\text{NO}_3^-)$ observations.

158
159 Following the preliminary work of Albertin et al. (2021), this study presents for the first time the simultaneous
160 measurements of the atmospheric NO_2 and NO_3^- multi-isotopic compositions. The sampling took place at high temporal
161 resolution (~ 3 h) in late February 2021 in an urban Alpine city. $\Delta^{17}\text{O}/\delta^{15}\text{N}$ data of NO_2 and NO_3^- , meteorological
162 parameters, and atmospheric observations (NO , NO_2 , O_3 , and PM) are collated in order to investigate diurnal N_r chemistry,
163 N fractionation effects and NO_x emissions. Our winter measurements extend the atmospheric NO_2 multi-isotopic
164 composition record which is only composed of spring measurements performed during a single day by Albertin et al. (2021).
165 The general aim of this case study is to test NO_2 -based isotopic approaches for tracing the origins and fate of NO_x , for
166 instance in urban areas on sub-daily time scales. The added value of $\Delta^{17}\text{O}(\text{NO}_2)$ measurements in N_r chemistry studies is
167 more critically assessed here than in Albertin et al. (2021) through the use of accurate NO_x measurements. Besides, using the
168 isotopic theoretical framework developed previously, we explore the potential benefits of combining isotopic observations of
169 NO_2 and NO_3^- to gain a more detailed and quantitative on the links between atmospheric N_r chemistry processes and
170 variability in NO_2 and NO_3^- isotopic composition. The framework used in inferring dominant NO_x emission sources from
171 NO_2 $\delta^{15}\text{N}$ measurements is also tested.

172 2 Material and methods

173 2.1 Study site and sample collection

174 The study was conducted in February 2021 in Chamonix-Mont-Blanc, France, (45°55'21" N, 6°52'11" E; altitude 1035 m
175 above sea level). This narrow (~2 km wide on average in Chamonix) 23 km Alpine valley of about 12,000 inhabitants is
176 surrounded by high-elevation mountains. The city can experience severe PM pollution events during the winter season,
177 mainly due to wood-combustion for domestic heating and road traffic (Chazette et al., 2005; Quimbayo-Duarte et al., 2021;
178 Weber et al., 2018; Aymoz et al., 2007). The study's sampling site was located at a CNRS (Centre National de la Recherche
179 Scientifique) facility in a residential area, 1.2 km south of the Chamonix city centre, and 1.4 km north of the Mont-Blanc
180 tunnel. Ambient air monitoring inlets and off-line gas and aerosol samplers were installed on the facility's terrace, 3 m above
181 the ground level. Over the campaign, the surface was partly covered with snow.

182

183 Atmospheric particles (aerosols) were collected using a high-volume sampler (Digitel®, DH77, total suspended particle
184 inlet, 1 m³ min⁻¹) and glass fiber (GF) filters (Whatman®, 150 mm-diameter). Evaluating the collection efficiency of total
185 NO₃⁻ has long been debated (e.g., Schaap et al., 2002; Appel et al., 1980) and, although not free from sampling artefacts
186 (e.g., potential volatilisation of HNO₃ after exposure to ambient air), GF filters have been used on several times to study
187 nitrate isotopes, mainly in coastal sites (e.g., Savarino et al., 2007; Michalski et al., 2003; Morin et al., 2009; Frey et al.,
188 2009; Morin et al., 2007a; Patris et al., 2007; Vicars et al., 2013). Under these conditions, the aerosol alkalinity is supposed
189 to allow the collection of HNO₃ (Prospero and Savoie, 1989). In our case, as the ambient air in Chamonix is expected to be
190 free of sea salt, the GF filters were not washed before use in order to keep the initial NaCl coating inherited from the filter
191 manufacturing process. Therefore, in addition to *p*-NO₃⁻, we are confident that the high GF filter NaCl loading allowed the
192 quantitative collection of HNO₃ at our site, as it has been shown previously in the literature (Appel et al., 1981; see also our
193 reply and data to the comments of Reviewer #2 on this specific issue). Two field blanks were performed to evaluate the
194 initial content of trace elements and possible contamination during handling. Atmospheric NO₂ was collected concurrently to
195 filter samples using a pre-cleaned honeycomb denuder tube coated with a mixture of 2.5 M KOH (in methanol) and ultrapure
196 guaiacol inserted into a ChemComb® 3500 speciation cartridge (Thermo Scientific®, USA). A second coated denuder was
197 placed in series into the cartridge to check for NO₂ breakthrough. After sampling, denuders were rinsed with 10 mL of
198 deionised water to solubilised trapped NO₂. Detailed information on the denuder sampling protocol is available in Albertin et
199 al. (2021). Similar to blank filters, two blank denuders were performed. Blank filters and denuders were subjected to same
200 handling, storage, and analytical treatment as field samples. Filters and denuder extractions were stored and transported
201 frozen to IGE (Grenoble, France) for analysis.

202

203 Following the objective to investigate the diurnal isotopic composition of NO₂ and NO₃⁻, denuder and filter samplings
204 were conducted continuously for 24 hours with sampling time steps ranging from 1:30 to 7:30. During the day, denuder and

205 filter samplings were synchronised. At night, two filter samplings were performed while three sets of denuder tubes were
206 collected. This sampling protocol was conducted during two non-consecutive days, from 19 February 2021 21:00 local time
207 (LT) to 20 February 2021 21:00 LT (sampling period #1 = SP 1) and from 24 February 2021 7:30 LT to 25 February 2021
208 7:30 LT (sampling period #2 = SP 2).

209 **2.2 Chemical and isotopic analysis**

210 Concentrations of major ions from filter extractions in deionised water were determined by ion chromatography
211 (Thermo Scientific™ Dionex™ Integrion™ HPIC). Reported to the total filter surface, the NO_3^- contribution from blank
212 filters represented on average (8 ± 9) % of sampled NO_3^- . Atmospheric mass concentrations (expressed in $\mu\text{g m}^{-3}$) were
213 calculated as the ratio of the total ion filter loading (corrected for the blank contribution) to the total volume of air pumped
214 through the filter at STP conditions. NO_2^- concentration in denuder extractions were first estimated using the Griess-
215 Saltzmann reaction and UV-Vis spectrometry at 544 nm. Even though the eluted matrix can interfere with colorimetric
216 analyses, measured concentrations on first denuder tubes were relatively well correlated with ambient NO_2 measurements
217 during atmospheric sampling and allowed to give indications on field blanks and on the volume needed to perform isotopic
218 analysis.

219

220 Isotopic analyses were performed using an isotope ratio mass spectrometer (IRMS, Thermo Finnigan™ MAT 253) for
221 analyses of $^{15}\text{N}/^{14}\text{N}$, $^{17}\text{O}/^{16}\text{O}$, and $^{18}\text{O}/^{16}\text{O}$ in NO_3^- and NO_2 samples. Briefly, NO_3^- from filter extractions were converted
222 into gaseous N_2O by the bacterial denitrifier method (Sigman et al., 2001; Casciotti et al., 2002; Kaiser et al., 2007) in which
223 ≈ 100 nmol of NO_3^- ions were injected into a 2 mL of a bacteria medium (strain of *Pseudomonas aureofaciens*) under
224 anaerobic conditions. NO_2 denuder extractions were treated separately with the azide method (McIlvin and Altabet, 2005;
225 Albertin et al., 2021) in which 2 mL of a sodium azide 2M / acetic acid 100 % buffer were injected into ≈ 100 nmol of NO_2^-
226 allowing quantitative conversion into N_2O . For both filter and denuder extractions, ions were converted into N_2O which was
227 further thermally decomposed into O_2 and N_2 in a gold tube heated at 850 °C. Then, O_2 and N_2 molecules were separated on
228 a chromatography column and sent separately into the IRMS for the dual analysis of O and N isotopes (see Morin et al.,
229 2009 for more details on the analytical line). The isotopic composition of NO_3^- samples was analysed in triplicate (the mean
230 value of replicate measurements and the associated repeatability are reported in Table S2 in the Supplement). The limited
231 amount of NO_2 samples did not allow for replicate measurements. From UV-vis analysis, all NO_2 samples presented a
232 negligible blank (< 4 %; mean of 1.7 nmol ml^{-1}) except for the sample collected between 13:30 and 16:30 LT during SP 2
233 which shown a blank around (14.0 ± 1.4) %. Therefore, the measured $\Delta^{17}\text{O}$ of this sample was corrected for blank effect
234 assuming that the contaminated NO_2^- possessed a $\Delta^{17}\text{O} = 0$ ‰. No correction from this blank effect was applied on the $\delta^{15}\text{N}$
235 measurements of NO_2 because the $\delta^{15}\text{N}$ fingerprint of the contamination could not be characterised. This uncertainty is
236 propagated in the calculations of Section 3 and considered in the discussions. Possible isotopic changes resulting from the

237 conversion and analysis process of NO_3^- and NO_2 samples were evaluated using international NO_3^- and NO_2^- isotopic
238 reference materials, respectively (Table S3 in the Supplement). Accuracy of the analytical method was estimated as the
239 standard deviation (σ) of the residuals between measurements of the reference materials and their expected values. In our
240 study, average measurement uncertainties on $\delta^{15}\text{N}$, $\delta^{17}\text{O}$, $\delta^{18}\text{O}$, and $\Delta^{17}\text{O}$ were estimated to be $\pm 0.3\text{‰}$, $\pm 0.9\text{‰}$, $\pm 1.3\text{‰}$, and
241 $\pm 0.4\text{‰}$, respectively, for NO_3^- samples and $\pm 0.3\text{‰}$, $\pm 0.4\text{‰}$, $\pm 0.9\text{‰}$, and $\pm 0.3\text{‰}$, respectively, for NO_2 samples. Detailed
242 information about the calibration procedure can be found in Morin et al. (2009) and in Albertin et al. (2021) for NO_3^- and
243 NO_2 samples, respectively.

244 **2.3 Ancillary data**

245 During atmospheric samplings, surface NO_x mixing ratios were measured at the study site using an incoherent broadband
246 cavity-enhanced absorption spectrometer for NO_2 (IBBCEAS; Barbero et al., 2020) and an optical-feedback cavity-enhanced
247 absorption spectrometer for NO (OFCEAS; Richard et al., 2018). PM concentrations (PM_{10} and $\text{PM}_{2.5}$) were monitored by an
248 optical particle counter (GRIMM[®], EDM 164). O_3 mixing ratio was monitored at the local air quality monitoring site located
249 a kilometre north of the sampling site (Environnement SA[®], O3 42M; <https://www.atmo-auvergnerhonealpes.fr/>, last access:
250 5 November 2021). Surface temperature (T_{surface}) and relative humidity (RH) were measured by a portable logger (Tinytag,
251 TGP-4500, Gemini Data Loggers) located at the air quality monitoring site. Vertical temperatures were measured from 11
252 similar loggers fixed along the Plan-Praz cable car ($45^\circ 55' 39''$ N, $6^\circ 51' 55''$ E) from 1098 to 2021 m above sea level (data
253 obtained from personal communications with C. Coulaud, IGE). The NO_2 photolysis rate (J_{NO_2}) was calculated for the two
254 sampling periods using a photochemical boxmodel (CiTTyCAT version 2.02; Galeazzo et al., 2018; Pugh et al., 2012) using
255 the Fast-J photolysis scheme of Wild et al. (2000) and a surface albedo fixed to 0.65, a value representative of a snow-
256 covered surface (average value between fresh and old snow; more details can be found in Text S1 in the Supplement).

257 **2.4 Interpretation framework for isotopic signals**

258 In this section, we briefly state the key concepts and equations necessary to interpret isotopic signals measured in NO_2 and
259 NO_3^- . A more detailed description and complete equation derivations can be found in cited references.

260 **2.4.1 $\Delta^{17}\text{O}$ mass balance equations**

261 Because NO_2 and NO_3^- loss processes do not fractionate in terms of the oxygen mass-independent anomaly and considering
262 that each source reaction induces a transfer of $\Delta^{17}\text{O}$ to NO_2 and NO_3^- , one consider the mass conservation of $\Delta^{17}\text{O}$ during
263 fractionation processes in the N_r cycle. Hence, one can implement $\Delta^{17}\text{O}$ in the general mass balance equation of NO_2 and
264 NO_3^- . An overall expression of the time derivative of $\Delta^{17}\text{O}$ in the species X ($\Delta^{17}\text{O}(\text{X})$; with $\text{X} = \text{NO}_2$ or NO_3^-) is derived as a
265 function of its deviation from $\Delta^{17}\text{O}$ transferred through each production channel i (P_i) ($\Delta^{17}\text{O}_i(\text{X})$), weighted according to the
266 relative contributions of the production channels (Vicars et al., 2013):

$$\frac{d}{dt}(\Delta^{17}\text{O}(\text{X})) = \frac{1}{\tau(\text{X})} \times \sum_i \frac{P_i}{\sum_i P_i} \times (\Delta^{17}\text{O}_i(\text{X}) - \Delta^{17}\text{O}(\text{X})) \quad (2)$$

267 where P_i expresses reaction rate constant times the atmospheric concentrations of reacting species, and τ is the atmospheric
 268 lifetime of the species X at steady state ($\tau = [\text{X}]/\sum_i P_i$ with $[\text{X}]$ being the atmospheric mixing ratio of the species X).

269

270 During the day, the rapid photochemical cycling of NO_x (Reactions R1–R4) leads to an isotopic equilibrium between
 271 NO and NO_2 , i.e., $\Delta^{17}\text{O}(\text{NO}) \approx \Delta^{17}\text{O}(\text{NO}_2)$ (Michalski et al., 2014). Therefore, using the steady state approximation, and
 272 considering $\text{NO} + \text{O}_3$ (Reaction R3) and $\text{NO} + \text{RO}_2$ (Reaction R4) as the main sources of NO_2 at our site, the overall daytime
 273 $\Delta^{17}\text{O}$ in NO_2 can be expressed by:

$$\Delta^{17}\text{O}_{\text{day}}(\text{NO}_2) \approx T_{\text{NO}+\text{O}_3} \times \Delta^{17}\text{O}_{\text{NO}+\text{O}_3}(\text{NO}_2) \quad (3)$$

274 where $\Delta^{17}\text{O}_{\text{NO}+\text{O}_3}(\text{NO}_2)$ is the O_3 isotopic anomaly transferred to NO through Reaction (R3) (Savarino et al., 2008). $T_{\text{NO}+\text{O}_3}$,
 275 sometimes named A in the literature, represents the proportion of O atoms originating from O_3 in NO_2 , and hence the relative
 276 importance of Reaction (R3) in the conversion of NO into NO_2 (Michalski et al., 2003; Morin et al., 2007b; Albertin et al.,
 277 2021):

$$T_{\text{NO}+\text{O}_3} = \frac{k_{\text{NO}+\text{O}_3}[\text{O}_3]}{k_{\text{NO}+\text{O}_3}[\text{O}_3] + k_{\text{NO}+\text{RO}_2}[\text{RO}_2]} \quad (4)$$

278 where $k_{\text{NO}+\text{O}_3}$ and $k_{\text{NO}+\text{RO}_2}$ are the kinetic constants of Reactions (R3) and (R4), respectively. The kinetic constants used in
 279 this study are listed in Table A1 in the Appendix. At night, considering that (1) $\Delta^{17}\text{O}(\text{NO}) \approx 0$ ‰ (NO_x emission without
 280 NO_2 recycling), (2) no $\Delta^{17}\text{O}$ equilibrium between NO and NO_2 (no photochemical cycling), and (3) O_3 is the main oxidant of
 281 NO (no nighttime production of RO_2), $\Delta^{17}\text{O}(\text{NO}_2)$ is determined by the $\Delta^{17}\text{O}$ transfer via Reaction (R3) and by the nighttime
 282 residuals of NO_2 formed during the previous daytime hours (Albertin et al., 2021) following:

$$\Delta^{17}\text{O}_{\text{night}}(\text{NO}_2) \approx x \times \Delta^{17}\text{O}_{\text{day}}(\text{NO}_2) + \frac{(1-x)}{2} \times (\Delta^{17}\text{O}_{\text{NO}+\text{O}_3}(\text{NO}_2) + \Delta^{17}\text{O}(\text{NO})) \quad (5)$$

283 where x is the fraction of NO_2 formed during the day to the total NO_2 measured at night.

284

285 At our sampling site, we hypothesise Reaction (R5) (OH pathway) and Reactions (R6)–(R8) (N_2O_5 pathway) as the
 286 main daytime and nighttime NO_3^- production channels, respectively. At steady state, from Eq. (2), we derive general

287 expressions for $\Delta^{17}\text{O}$ in NO_3^- during the day and night, associated with the OH and N_2O_5 pathways, respectively (Alexander
288 et al., 2020):

$$\Delta^{17}\text{O}_{\text{day}}(\text{NO}_3^-) \approx \frac{2}{3} \times \Delta^{17}\text{O}_{\text{day}}(\text{NO}_2) \quad (6)$$

$$\Delta^{17}\text{O}_{\text{night}}(\text{NO}_3^-) \approx \frac{2}{3} \times \Delta^{17}\text{O}_{\text{night}}(\text{NO}_2) + \frac{1}{6} \times \Delta^{17}\text{O}_{\text{NO}_2+\text{O}_3}(\text{NO}_3) \quad (7)$$

289 where $\Delta^{17}\text{O}_{\text{NO}_2+\text{O}_3}(\text{NO}_3)$ is the ^{17}O -excess transfer from O_3 to NO_3 during Reaction (R6) (Berhanu et al., 2012). Without
290 wet scavenging, dry deposition is the main sink of NO_3^- (Park et al., 2004). Assuming a mean NO_3^- deposition velocity of
291 0.5 cm s^{-1} (mean value of the dry deposition velocities of HNO_3 and $p\text{-NO}_3^-$; Zhang et al., 2009), and considering the
292 maximum daytime and minimum nighttime boundary layer heights of 500 and 100 m above ground level, respectively
293 (estimations based on measured vertical temperature profiles; Fig. S2 in the Supplement), the estimated residence time of
294 NO_3^- against dry deposition can reach up to 28 hours during the day, and 6 hours at night (Table B1). Therefore, on sub-
295 daily time scales, the ^{17}O -excess in NO_3^- during the day is more likely to reflect a combination of daytime and nighttime
296 production processes than during the night. Note that, our estimated residence times for NO_3^- against dry deposition are
297 upper limits as they represent the time required to reduce by a factor e the concentration of NO_3^- present at the top of the
298 boundary layer; NO_3^- close to the surface would have a much shorter residence time.

299 2.4.2 Nitrogen isotopic fractionation effects

300 Each source of NO_x generates a $\delta^{15}\text{N}$ fingerprint which depends on the type and conditions (temperature and pressure) of
301 combustion, and on the type of fuel (e.g., coal, oil, gas) (Heaton, 1990; Felix et al., 2012; Fibiger and Hastings, 2016;
302 Walters et al., 2015a, b; Yu and Elliott, 2017; Miller et al., 2018). The mean $\delta^{15}\text{N}$ of NO_x ($\delta^{15}\text{N}(\text{NO}_x)$) emitted in the
303 atmosphere results from the sum of each NO_x emission $\delta^{15}\text{N}$ fingerprint weighted by their relative contribution to the total
304 NO_x emissions. Once in the atmosphere, NO_x is subjected to oxidation processes and isotopic exchanges that alter the initial
305 $\delta^{15}\text{N}(\text{NO}_x)$. As a result, $\delta^{15}\text{N}$ in NO_2 and in NO_3^- is a complex function of both the $\delta^{15}\text{N}$ signature of NO_x emissions and N
306 isotopic effects. These latter can be categorised into three groups: (1) the equilibrium isotope effect (EIE), (2) the kinetic
307 isotope effect (KIE), and (3) the photochemical isotope fractionation effect (PHIFE) (Miller and Yung, 2000; Young et al.,
308 2002). The magnitude of these isotopic effects is quantified as ^{15}N enrichment factor (ϵ), which is defined as $(\alpha - 1)$, where α
309 represents the N isotopic fractionation factor.

310

311 A general expression for $\delta^{15}\text{N}(\text{NO}_2)$ can be derived as a function of a factor F_{N} which represents the overall N isotopic
 312 fractionation effects between NO_x emissions and NO_2 (expressed in ‰), the fraction of NO_2 with respect to NO_x ($f_{\text{NO}_2} =$
 313 $[\text{NO}_2]/[\text{NO}_x]$), and of $\delta^{15}\text{N}(\text{NO}_x)$ (Albertin et al., 2021; Li et al., 2020):

$$\delta^{15}\text{N}(\text{NO}_2) = F_{\text{N}} \times (1 - f_{\text{NO}_2}) + \delta^{15}\text{N}(\text{NO}_x) \quad (8)$$

314 Therefore, the ^{15}N isotopic shift between $\delta^{15}\text{N}(\text{NO}_2)$ and $\delta^{15}\text{N}(\text{NO}_x)$ is given by:

$$\delta^{15}\text{N}(\text{NO}_2) - \delta^{15}\text{N}(\text{NO}_x) = \Delta^{15}(\text{NO}_2 - \text{NO}_x) = F_{\text{N}} \times (1 - f_{\text{NO}_2}) \quad (9)$$

315 Physico-chemical processes between NO and NO_2 can preferentially promote or deplete ^{15}N in NO_2 with respect to emissions
 316 of NO_x (i.e., $\delta^{15}\text{N}(\text{NO}_2) \neq \delta^{15}\text{N}(\text{NO}_x)$). The importance of this fractionation shift is modulated by the factor $(1 - f_{\text{NO}_2})$. When
 317 NO is almost entirely converted into NO_2 ($f_{\text{NO}_2} \approx 1$), N fractionation effects can be neglected (i.e., $\delta^{15}\text{N}(\text{NO}_2) \approx \delta^{15}\text{N}(\text{NO}_x)$).

318 From samples collected at Jülich, Germany, Freyer et al. (1993), observed for the first time the linear relation described
 319 by Eq. (8), and set the theoretical framework to interpret $\delta^{15}\text{N}$ variabilities in atmospheric NO_2 . They showed that the
 320 observed seasonal variation of $\delta^{15}\text{N}(\text{NO}_2)$ was driven by N fractionation effects (represented in the F_{N} factor) caused by
 321 photochemistry and isotopic equilibrium. Based on this work, and that of Li et al. (2020), Albertin et al. (2021) derived an
 322 expression of F_{N} during the day assuming that the NO - NO_2 system is in isotopic equilibrium (steady-state):

$$(F_{\text{N}})_{\text{day}} \approx \frac{\alpha_{\text{LCIE}}^* A^*_{\text{day}} + (\alpha_{\text{EIE}(\text{NO}_2/\text{NO})} - 1)}{A^*_{\text{day}} + 1} \quad (10)$$

323 with $\alpha_{\text{LCIE}}^* = \alpha_{\text{KIE}(\text{NO}+\text{O}_3)} - \alpha_{\text{PHIFE}}$

324 and $A^*_{\text{day}} = \frac{J_{\text{NO}_2}}{k_{\text{NO}+\text{NO}_2}[\text{NO}]}$

325 where α_{LCIE}^* is the fractionation factor of combined KIE and PHIFE (LCIE is for Leighton Cycle Isotope Effect), and
 326 $\alpha_{\text{EIE}(\text{NO}_2/\text{NO})}$ is the EIE fractionation factor between NO and NO_2 . $\alpha_{\text{EIE}(\text{NO}_2/\text{NO})}$ and $\alpha_{\text{KIE}(\text{NO}+\text{O}_3)}$ are temperature dependent
 327 and can be calculated following the theoretical approach of Walters and Michalski (2015) (Table D1). From calculations
 328 based on the zero point energy of $^{15}\text{NO}_2$ and the absorption cross section of $^{14}\text{NO}_2$, α_{PHIFE} is estimated to vary between
 329 1.0020 and 1.0042 for a range of solar zenith angles between 90° and 0° (Fang et al. 2021). In this study we use a mean
 330 value of α_{PHIFE} at 1.0031. A^*_{day} is defined as the ratio of the NO_2 lifetime with respect to isotopic exchanges over the
 331 daytime NO_2 chemistry lifetime. J_{NO_2} is the NO_2 photolysis rate, $k_{\text{NO}+\text{O}_3}$ is the rate constant of Reaction (R3), and $k_{\text{NO}+\text{NO}_2}$

332 is the rate constant of the isotopic exchange $^{15}\text{NO}_2 + ^{14}\text{NO} \rightarrow ^{14}\text{NO}_2 + ^{15}\text{NO}$. During the day, $\Delta^{15}(\text{NO}_2 - \text{NO}_x)$ varies
 333 according to the environmental conditions. In low- NO_x conditions (e.g., remote and polar regions) $\Delta^{15}(\text{NO}_2 - \text{NO}_x)$ is
 334 predicted to be controlled by LCIE factors ($A^*_{\text{day}} \gg 1$), whereas an EIE-dominated regime ($A^*_{\text{day}} \ll 1$) is expected in
 335 polluted environments (high- NO_x conditions). At night, J_{NO_2} and α_{PHIFE} are null and A^*_{night} is defined as the ratio of NO
 336 lifetime with respect to isotopic exchange with NO_2 to NO chemical lifetime at night $\left(A^*_{\text{night}} = \frac{k_{\text{NO}+\text{O}_3}[\text{O}_3]}{k_{\text{NO}+\text{NO}_2}[\text{NO}_2]}\right)$. In this study,
 337 we consider only one particular case with $A^*_{\text{night}} \ll 1$, which means that isotopic exchanges are much faster than NO
 338 oxidation by O_3 . In this scenario, KIE effects are negligible compared to EIE effects and $(F_{\text{N}})_{\text{night}}$ can be expressed as:

$$(F_{\text{N}})_{\text{night}} \approx \frac{(\alpha_{\text{EIE}(\text{NO}_2/\text{NO})} - 1)}{\alpha_{\text{EIE}(\text{NO}_2/\text{NO})}} \quad (11)$$

339 The complete derivation of Eqs. (10) and (11) is given in Albertin et al. (2021).

340

341 KIE and EIE are also expected during the conversion of NO_2 to NO_3^- . The ^{15}N partitioning associated to isotopic
 342 equilibrium between N_2O_5 and NO_2 (Reaction R7) can be theoretically computed as a function of temperature (Walters and
 343 Michalski, 2015; Table D1). At 298 K, if N isotopic equilibrium is reached, N_2O_5 is predicted to have $\delta^{15}\text{N}$ values 27.6 ‰
 344 higher than NO_2 . Considering that the $\text{NO}_2/\text{NO}_3^-$ isotopic fractionation through the N_2O_5 pathway is solely controlled by
 345 EIE, NO_3^- is therefore expected to be enriched in ^{15}N relative to NO_2 . However, to date, no experimental study has reported
 346 on ^{15}N partitioning between atmospheric NO_2 and NO_3^- , and the fractionation factors are still being debated (Freyer 1991,
 347 Fang et al. 2021). The dominant NO_x to NO_3^- conversion processes considered in this study, along with corresponding $\Delta^{17}\text{O}$
 348 transfer factors and the known ^{15}N enrichment factors at 298 K (determined from both experimental and computational
 349 studies) are illustrated in Figure C1.

350 **3 Results and Discussion**

351 **3.1 Temporal variations of general atmospheric observations**

352 Surface temperatures during SP 1 and SP 2 show similar values, with a marked diurnal cycle (from $-2\text{ }^\circ\text{C}$ to $16\text{ }^\circ\text{C}$; Figure
 353 1). A positive temperature gradient with altitude is observed from late evening to morning. Surface temperature rises around
 354 midday and reaches a maximum at around 15:00 LT, resulting in a negative temperature gradient with altitude. In deep
 355 Alpine valleys, the diurnal variability of surface air temperature is strongly influenced by the temporal evolution of the
 356 boundary layer structure, particularly in winter with the formation of a surface layer inversion (Whiteman, 1982). As
 357 previously observed in Chamonix (Chazette et al., 2005), the nocturnal surface layer inversion regularly thickens during the
 358 night of the sampling periods. After sunrise, air masses warm up until the nocturnal inversion layer breaks down in the late

359 morning. Observed RH behaviour relatively correlates with the increase in temperature during the day, showing a rapid
360 decrease between mid-morning and early afternoon (from 96 % to 23 % and from 96 % to 30 % for SP 1 and SP 2,
361 respectively; Figure 1).

362

363 During SP 1 and SP 2, the mixing ratios of NO, NO₂ and O₃ exhibit diurnal patterns (Figure 1) typical in Chamonix in
364 late February (Figure S3 in the Supplement), and more generally in urban areas (Mayer, 1999). The highest NO level is
365 observed in the morning, peaking around 10:30 LT (82 nmol mol⁻¹ and 152 nmol mol⁻¹ for SP 1 and SP 2, respectively). The
366 concurrent increase in NO₂ and decrease in O₃ (down to 1 nmol mol⁻¹) can be attributed to Reaction (R3) (NO + O₃). NO_x
367 decreases in the late morning, likely due to a combination of lower emissions, NO₂ oxidation, and dilution effect.
368 Meanwhile, O₃ gradually recovers to ca. 30 nmol mol⁻¹, a typical winter background air level in Europe (Gaudel et al.,
369 2018). Due to local emissions, NO_x increases again from 16:00 LT, resulting in O₃ titration, and subsequently to an increase
370 in NO₂ (up to 40 nmol mol⁻¹). After 18:30 LT, NO remains low until the morning, and NO₂ decreases slowly until midnight,
371 stalls around 10 nmol mol⁻¹, and then rises again at 5:30 LT. After the late afternoon titration, O₃ gently recovers and stay
372 relatively low throughout the night likely due to a titration effect from nocturnal NO emissions which are confined in the
373 surface layer inversion.

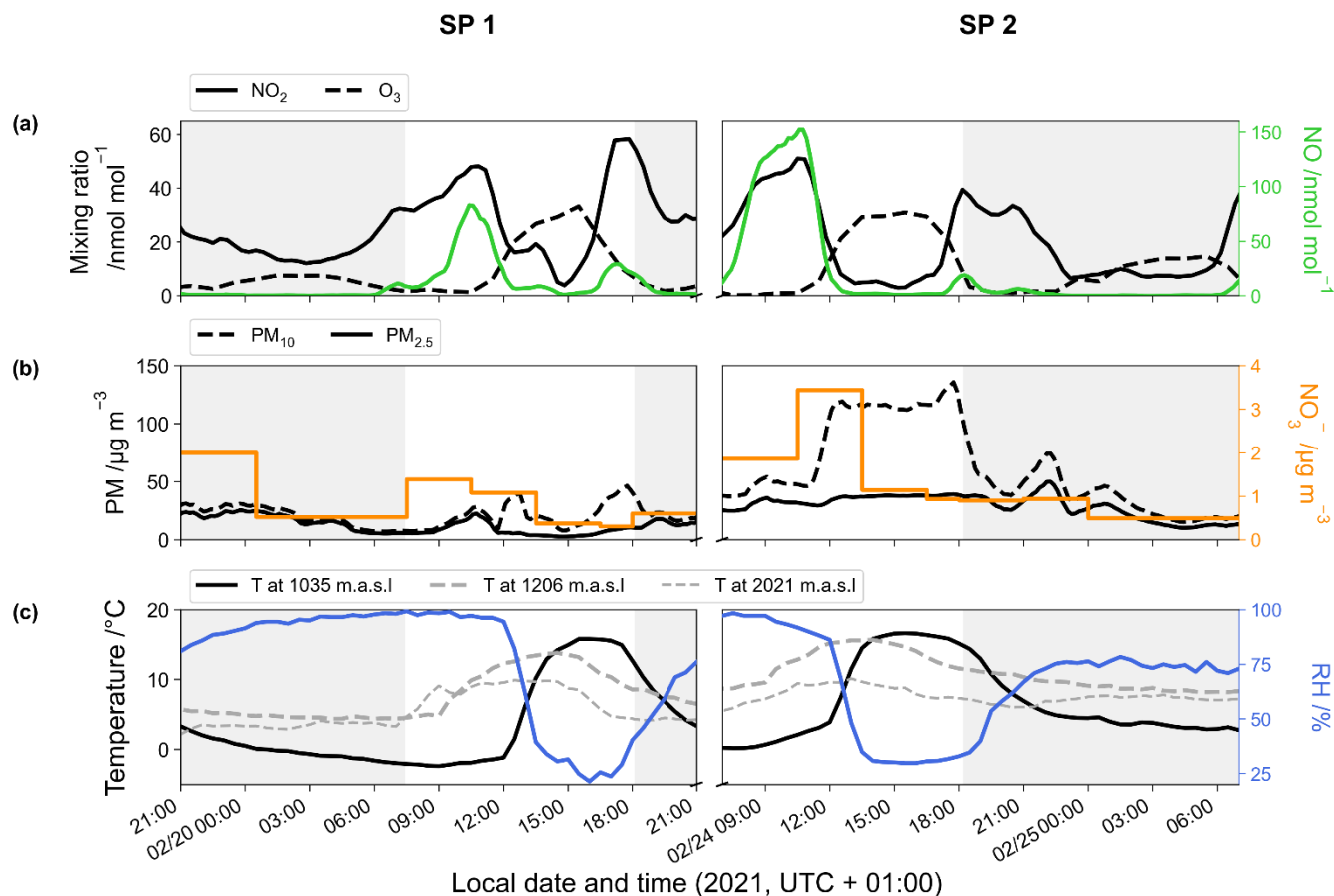
374

375 Both SP 1 and SP 2 show diurnal variations in PM mass concentrations (Figure 1), with morning and evening peaks
376 related to local emissions from traffic and home heating (Aymoz et al., 2007). PM₁₀ concentrations display an additional
377 increase at midday following the breakdown of the temperature inversion. At 12:30 LT, while PM₁₀ concentrations increase
378 moderately during SP 1 to reached 38.6 µg m⁻³, a sharp increase to 119 µg m⁻³ is observed during SP 2. Then PM₁₀
379 concentrations decrease during the afternoon of SP 1, but remain high during the afternoon of SP 2 until the surface
380 inversion layer forms. On average, PM₁₀ concentration is three times higher during SP 2 ((59.4 ± 37.6) µg m⁻³) than during
381 SP 1 ((20.6 ± 10.2) µg m⁻³). The considerable increase in PM₁₀ concentrations between SP 1 and SP 2 is likely to be
382 explained by a Saharan dust episode that started on February 23 (Fig. S3, S4, and S5 in the Supplement). Saharan dust
383 deposition is a well-known phenomenon in the Alps, which is characterised by a sudden increase of coarse particles, mainly
384 composed of alumino-silicates as well as calcium and potassium (Angelisi and Gaudichet, 1991; Delmas, 1994; Di Mauro et
385 al., 2019; Goudie and Middleton, 2001; Greilinger et al., 2018; Schwikowski et al., 1995; Sodemann et al., 2006).

386

387 The NO₃⁻ mass concentration varies from 0.3 µg m⁻³ to 3.4 µg m⁻³, with an average of (0.9 ± 0.6) µg m⁻³ for SP 1 and
388 of (1.2 ± 0.9) µg m⁻³ for SP 2 (Figure 1). During both sampling periods, NO₃⁻ concentration is within the range of previous
389 observations made in Chamonix in winter (Allard, 2018). NO₃⁻ shows a distinctive peak at 3.4 µg m⁻³ during SP 2 between
390 10:30 and 13:30 LT, correlated with the PM₁₀ surge. During transport, dust can undergo heterogeneous uptake and
391 conversion of gases on its surface, leading to the inclusion of secondary species such as NO₃⁻, sulfate, and ammonium

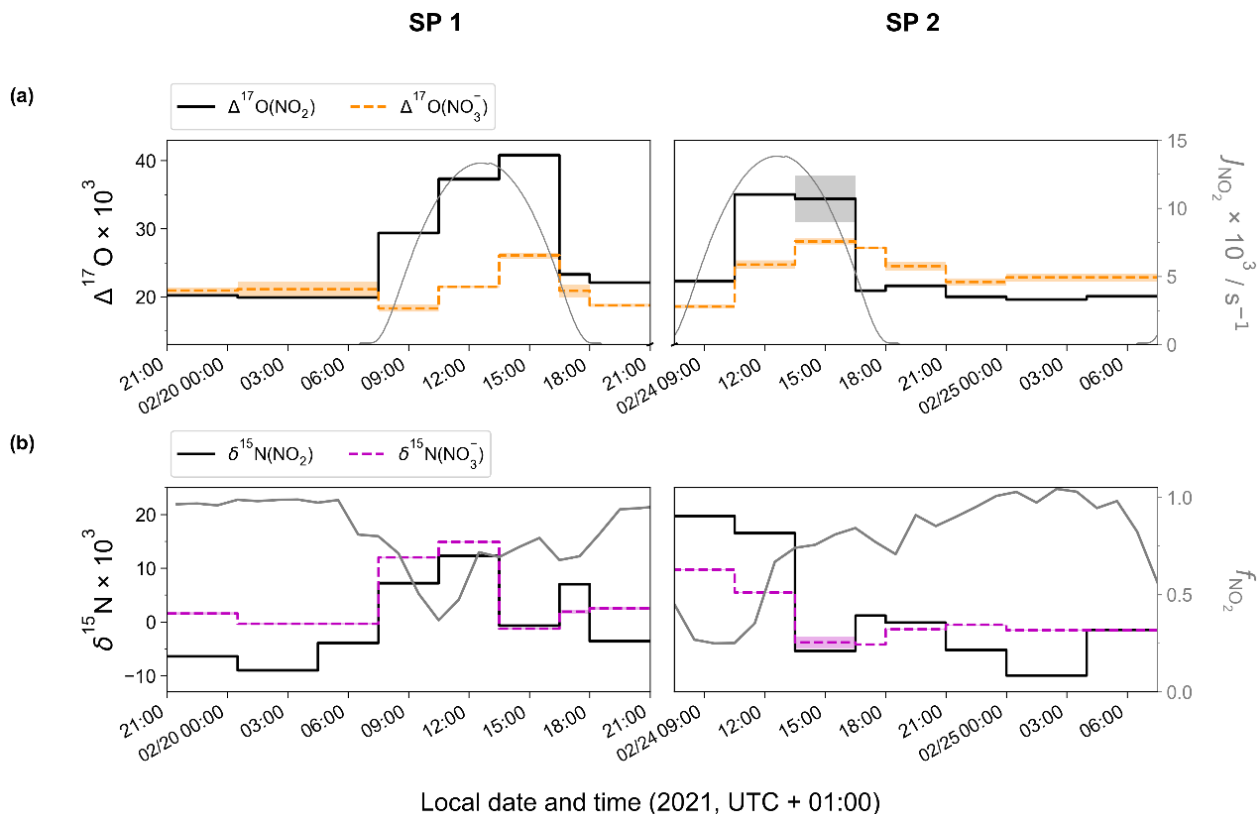
392 (Usher et al., 2003). NO_3^- on dust results mainly from HNO_3 uptake and heterogeneous reactions of N_2O_5 (see Usher et al.,
 393 2003 for a review and references therein). Mineral dust is believed to significantly contribute to NO_3^- formation and size
 394 distribution, particularly in regions close to dust emission sources (Karydis et al., 2016). However, the origin of NO_3^- during
 395 SP 2 at our site remains unclear and could be attributed to the advection of both nitrated-dust particles formed through
 396 heterogeneous processes during transport and anthropogenic fine particles (Aymoz et al. 2004).
 397



398
 399 **Figure 1.** Temporal evolution of the 1-hour rolling mean of (a) NO_2 (black line), O_3 (dashed line), and NO (green line) mixing ratios, (b)
 400 PM (dashed line for PM_{10} and solid line for $\text{PM}_{2.5}$) and NO_3^- (orange horizontal line) mass concentrations, and (c) temperature at the surface (black line), at 1206 m (dashed grey line), and at 2021 m (light dashed grey line) and surface relative humidity (blue line). Data
 401 were collected during the two sampling periods (SP 1 and SP 2) in Chamonix. Grey backdrop shaded areas represent the nighttime (sunset
 402 to sunrise).
 403

404
 405 Figure 2 shows the temporal evolution of measured $\Delta^{17}\text{O}$ and $\delta^{15}\text{N}$ of NO_2 and NO_3^- in Chamonix during the two
 406 sampling periods (SP 1 and SP 2). All isotopic data used in this study are reported in Table S1 and Table S2 in the
 407 Supplement. In the following analysis, first we describe $\Delta^{17}\text{O}(\text{NO}_2)$ measurements and gives interpretation in light of NO_x

408 chemistry cycling (Section 3.2). Then, an analysis of $\Delta^{17}\text{O}(\text{NO}_3^-)$ measurements is proposed aggregating daytime and
 409 nighttime periods and comparing them with $\Delta^{17}\text{O}(\text{NO}_3^-)$ estimates derived from $\Delta^{17}\text{O}(\text{NO}_2)$ measurements and $\Delta^{17}\text{O}$ mass
 410 balance for major chemical processes (Section 3.3). In light of these results and atmospheric conditions during SP 1 and SP
 411 2, sub-daily $\Delta^{17}\text{O}(\text{NO}_3^-)$ dynamics are investigated. In Section 3.4, N fractionation effects in the NO_x cycle are quantified,
 412 and the dominant NO_x emission source is identified. The dynamics of $\delta^{15}\text{N}(\text{NO}_3^-)$ is also described and its use to trace NO_x
 413 emission sources and oxidation processes is discussed.



414

415 **Figure 2.** Temporal evolution of observed (a) $\Delta^{17}\text{O}$ and (b) $\delta^{15}\text{N}$ of atmospheric NO_2 (top and bottom solid black horizontal line) and
 416 NO_3^- (top orange and bottom magenta horizontal dashed line) in Chamonix (length of horizontal line = sampling period, shaded area =
 417 overall analytical error). The NO_2 photolysis rate (J_{NO_2} , top grey line) is from CiTTYCAT boxmodel output. f_{NO_2} ($f_{\text{NO}_2} = [\text{NO}_2] / ([\text{NO}_2]$
 418 $+ [\text{NO}])$; bottom grey line) is calculated from hourly mean mixing ratio of NO and NO_2 .

419 3.2 $\Delta^{17}\text{O}$ of NO_2 and NO_x diurnal cycling

420 Over the course of SP 1 and SP 2, $\Delta^{17}\text{O}(\text{NO}_2)$ shows a large diurnal variability (from 19.6 ‰ to 40.8 ‰) with a weighted
 421 mean \pm one standard deviation of (25.2 ± 7.1) ‰. $\Delta^{17}\text{O}(\text{NO}_2)$ values during the day (7:30–18:00 LT, (28.5 ± 7.3) ‰) are
 422 significantly higher (p -value = 0.002, $n = 16$) than during the night (18:00–7:30 LT, (20.8 ± 1.0) ‰). By day, $\Delta^{17}\text{O}(\text{NO}_2)$
 423 follows a similar increasing trend during SP 1 and SP 2, reaching a respective maximum of 40.8 ‰ between 13:30–16:30 LT

424 and 35.0 ‰ between 10h30–13h30 LT. For both sampling periods, after sunset, $\Delta^{17}\text{O}(\text{NO}_2)$ stabilises between 21:00 and
 425 7:30 LT at ca. 20 ‰. Using the same sampling methodology in a mid-latitude urban area in spring, Albertin et al. (2021)
 426 reported very similar $\Delta^{17}\text{O}(\text{NO}_2)$ values over the course of one day (20.5–39.2 ‰), following a comparable diurnal pattern.
 427 As presented above (Section 2.4.1), according to the ISS (isotopic steady state) framework, the variability of $\Delta^{17}\text{O}(\text{NO}_2)$
 428 reflects changes in the relative contributions of Reaction (R3) ($\text{NO} + \text{O}_3$) and Reaction (R4) ($\text{NO} + \text{RO}_2$) to the overall
 429 production of NO_2 . At our site, $\Delta^{17}\text{O}(\text{NO}_2)$ drops rapidly during the 16:30–18:00 LT interval to 23.3 ‰ and 20.9 ‰ during
 430 SP 1 and SP 2, respectively. Since, the isotope recycling rate in the $\text{NO}_x\text{-O}_3$ system is driven at first order by J_{NO_2} (Michalski
 431 et al., 2014), due to low solar radiation between 16:30–18:00 LT at our site, such a rapid drop of $\Delta^{17}\text{O}(\text{NO}_2)$ suggests that
 432 sampled NO_2 might not be at ISS anymore when the NO_2 photolysis is very slow, notably at the end of the day in winter.
 433 Therefore, we only consider that ISS holds between 7:30 and 16:30 LT in order to avoid the questionable end-of-the day
 434 measurements in our ISS-based analysis. At night (i.e., no ISS), the observed drop of $\Delta^{17}\text{O}(\text{NO}_2)$ in the early evening reflects
 435 the rapid replacement of NO_2 formed during the day by NO_2 produced during the night via the conversion of freshly emitted
 436 NO , in line with Eq. (5). Then, high NO_2 throughout the night, along with relatively low O_3 , supports observations of low
 437 $\Delta^{17}\text{O}(\text{NO}_2)$ at night (i.e., ≈ 20 ‰).

438

439 Using Eq. (3), we derive from $\Delta^{17}\text{O}(\text{NO}_2)$ observations the relative contribution of Reaction (R3) ($\text{NO} + \text{O}_3$) to
 440 Reaction (R4) ($\text{NO} + \text{RO}_2$) in the formation of NO_2 ($T_{\text{NO}+\text{O}_3}$):

$$T_{\text{NO}+\text{O}_3} = \frac{\Delta^{17}\text{O}_{\text{day}}(\text{NO}_2)}{\Delta^{17}\text{O}_{\text{NO}+\text{O}_3}(\text{NO}_2)} \quad (12)$$

441 Between 7:30 and 16:30 LT, $T_{\text{NO}+\text{O}_3}$ varies from 0.55 to 1.00 (Table 1), with a mean of 0.88 and 0.75 for SP 1 and SP 2,
 442 respectively. The $\text{NO} + \text{O}_3$ pathway is dominant between 13:30 and 16:30 LT, corresponding to the time when O_3 is highest
 443 (Figure 1). In contrast, the maximum contribution for the $\text{NO} + \text{RO}_2$ pathway is observed between 7:30 and 10:30 LT, when
 444 NO levels are high and rising continuously. Interestingly, previous studies reported a high sensitivity of RO_2 to changes in
 445 NO_x , particularly at high NO_x levels (Ren et al., 2006; Stone et al., 2012). Sources of RO_2 in wintertime are mainly driven by
 446 the production of OH radicals from HONO photolysis, alkene ozonolysis, and formaldehyde photolysis (Tan et al., 2018).
 447 During winter, HONO plays a crucial role in $\text{NO}_x/\text{O}_3/\text{RO}_2$ chemistry, particularly in the morning, as its photolysis can
 448 potentially accelerate daytime oxidation processes, leading to increased RO_2 production (Alicke et al., 2003; Aumont et al.,
 449 2003). Direct emissions from vehicle exhaust could be significant a source of VOCs and HONO at our site (Brulfert et al.,
 450 2005; Gu et al., 2019; Kirchstetter et al., 1996; Kurtenbach et al., 2001; Liu et al., 2023). Heterogeneous processes on ground
 451 surfaces and aerosols can also contribute to HONO formation (Aumont et al., 2003). In addition, snowpack releases may also

452 be a potential source of HONO (Grannas et al., 2007), as detected in Paris after a snow event, which could significantly
 453 impact the urban OH budget (Michoud et al. 2015).

454

455 Following the approach of Albertin et al. (2021), combining Eqs. (3) and (4) allows to derive RO₂ mixing ratio from
 456 observed $\Delta^{17}\text{O}(\text{NO}_2)$ and O₃ mixing ratio following:

$$[\text{RO}_2] = \frac{k_{\text{NO}+\text{O}_3}[\text{O}_3]}{k_{\text{NO}+\text{RO}_2}} \left(\frac{\Delta^{17}\text{O}_{\text{NO}+\text{O}_3}(\text{NO}_2)}{\Delta^{17}\text{O}_{\text{day}}(\text{NO}_2)} - 1 \right) \quad (13)$$

457 Between 7:30 and 16:30 LT, we estimate an average RO₂ mixing ratio at our site of (0.88 ± 0.88) pmol mol⁻¹ and $(4.92 \pm$
 458 $5.16)$ pmol mol⁻¹ during SP 1 and SP 2, respectively (Table 1). Studies conducted in urban winter environments reported
 459 RO₂ measurements at a few pmol mol⁻¹ (Ren et al., 2006; Emmerson et al., 2005; Tan et al., 2018; Kanaya et al., 2007), in
 460 good agreement with our estimations. Similarly, RO₂ mixing ratios derived by Albertin et al. (2021) from observed
 461 $\Delta^{17}\text{O}(\text{NO}_2)$ in spring (mean of (13.8 ± 11.2) pmol mol⁻¹) were also found to be in line with studies conducted in the same
 462 season. The fact that our isotopic inference of RO₂ mixing ratios carried out in two different seasons (winter and spring) are
 463 both comparable to direct in situ RO₂ measurements confirm the sensitivity of our method in probing the NO_x/O₃/RO₂
 464 chemical dynamics. We think that our method may be very valuable in deciphering oxidation processes of N_r species, down
 465 to sub-daily temporal scales. Nonetheless, we recognise that without concurrent in situ measurements of RO₂ and
 466 $\Delta^{17}\text{O}(\text{NO}_2)$, it is not possible to validate unambiguously the quantitative estimation of RO₂ levels with our method.

467

Sampling interval (start - end)	$T_{\text{NO}+\text{O}_3}$	RO ₂ /pmol mol ⁻¹
SP 1		
20/02 07:30 - 20/02 10:30	0.72 ± 0.01	0.86 ± 0.75
20/02 10:30 - 20/02 13:30	0.91 ± 0.01	1.77 ± 0.36
20/02 13:30 - 20/02 16:30	1.00 ± 0.01	0.00 ± 0.91
<i>Mean</i>	<i>0.88</i>	<i>0.88</i>
<i>Std dev.</i>	<i>0.14</i>	<i>0.88</i>
SP 2		
24/02 07:30 - 24/02 10:30	0.55 ± 0.01	0.58 ± 1.67
24/02 10:30 - 24/02 13:30	0.86 ± 0.01	3.56 ± 0.50
24/02 13:30 - 24/02 16:30	0.84 ± 0.08	10.63 ± 6.75
<i>Mean</i>	<i>0.75</i>	<i>4.92</i>
<i>Std dev.</i>	<i>0.18</i>	<i>5.16</i>

468

469 **Table 1.** $T_{\text{NO}+\text{O}_3}$ and RO₂ mixing ratio (mean value \pm overall uncertainty) derived from the isotopic measurements.

470

471 At this point, it is important to recall that the choice of the $\Delta^{17}\text{O}_{\text{NO}+\text{O}_3}(\text{NO}_2)$ in Eq. (12) is of a particular importance
 472 for quantifying $T_{\text{NO}+\text{O}_3}$ (as for RO_2). In the literature, $\Delta^{17}\text{O}_{\text{NO}+\text{O}_3}(\text{NO}_2)$ varies between 35 ‰ and 41 ‰ (Michalski et al.,
 473 2003; Savarino et al., 2016; Vicars et al., 2012; Zhang et al., 2022b; Li et al., 2022a). This relatively wide range of values is
 474 partly a result of some confusion in defining $\Delta^{17}\text{O}_{\text{NO}+\text{O}_3}(\text{NO}_2)$, the $\Delta^{17}\text{O}$ transfer from O_3 to NO . Indeed, the term $\Delta^{17}\text{O}(\text{O}_3^*)$
 475 is sometimes erroneously used as the transfer function of $\Delta^{17}\text{O}$ from O_3 to NO_2 during Reaction (R3). $\Delta^{17}\text{O}(\text{O}_3^*)$ is actually
 476 defined as $\Delta^{17}\text{O}$ of O_3 terminal atoms and is also named $\Delta^{17}\text{O}(\text{O}_3)_{\text{term}}$ in the literature. As the $\Delta^{17}\text{O}$ in O_3 is borne by its
 477 terminal atoms, $\Delta^{17}\text{O}(\text{O}_3^*) = 1.5 \times \Delta^{17}\text{O}(\text{O}_3)_{\text{bulk}}$. However, $\Delta^{17}\text{O}_{\text{NO}+\text{O}_3}(\text{NO}_2)$ can be equal to $1.5 \times \Delta^{17}\text{O}(\text{O}_3)_{\text{bulk}}$ if only
 478 terminal atoms of O_3 reacts with NO . But laboratory experiments by Savarino et al. (2008) did show that O_3 does react with
 479 NO not solely with its terminal atoms but also, to a small but significant extent, with its central atom (probability of (8 ± 5)
 480 ‰ for the abstraction of central atoms during the reaction $\text{NO} + \text{O}_3$). Consequently, $\Delta^{17}\text{O}_{\text{NO}+\text{O}_3}(\text{NO}_2)$ is slightly lower than
 481 $1.5 \times \Delta^{17}\text{O}(\text{O}_3)_{\text{bulk}}$ and the $\Delta^{17}\text{O}_{\text{NO}+\text{O}_3}(\text{NO}_2)$ expression determined by Savarino et al. (2008) should be used:
 482 $\Delta^{17}\text{O}_{\text{NO}+\text{O}_3}(\text{NO}_2) = 1.18 \pm 0.07 \times \Delta^{17}\text{O}(\text{O}_3)_{\text{bulk}} + (6.6 \pm 1.5) \text{‰}$.

483

484 Assuming that their maximum measured daytime $\Delta^{17}\text{O}(\text{NO}_2)$ reflects the conversion of NO to NO_2 only through
 485 Reaction (R3) (i.e., $T_{\text{NO}+\text{O}_3} = 1$), Albertin et al. (2021) derived a $\Delta^{17}\text{O}_{\text{NO}+\text{O}_3}(\text{NO}_2)$ value of 39.2 ‰ from Eq. (3). Given the
 486 respective analytical uncertainties (around $\pm 1 \text{‰}$), their value is in very good agreement with the maximum daytime value of
 487 40.8 ‰ we observed in Chamonix. Similarly to Albertin et al. (2021), assuming that the highest daytime $\Delta^{17}\text{O}(\text{NO}_2)$ value at
 488 our site corresponds to $T_{\text{NO}+\text{O}_3} \approx 1$ leads to $\Delta^{17}\text{O}_{\text{NO}+\text{O}_3}(\text{NO}_2) = 40.8 \text{‰}$. Using the experimental $\Delta^{17}\text{O}_{\text{NO}+\text{O}_3}(\text{NO}_2)$ transfer
 489 function determined by Savarino et al. (2008), we estimate a bulk ^{17}O -excess of O_3 ($\Delta^{17}\text{O}(\text{O}_3)_{\text{bulk}}$) at $(29.0 \pm 2.2) \text{‰}$. This
 490 value is consistent with the range of direct $\Delta^{17}\text{O}(\text{O}_3)_{\text{bulk}}$ measurements at mid-latitudes (mean of $(26.2 \pm 1.3) \text{‰}$; Vicars
 491 and Savarino, 2014), although falling at the upper end of the range. Interestingly, Vicars and Savarino (2014) reported a
 492 significant peak in $\Delta^{17}\text{O}(\text{O}_3)_{\text{bulk}}$ during February-March in Grenoble, France (located 120 km southwest of Chamonix), based
 493 on year-round measurements with $\Delta^{17}\text{O}(\text{O}_3)_{\text{bulk}}$ values 2–3 ‰ higher than the annual mean of 26.2 ‰. Although the cause of
 494 increased values during this period is unknown, our derived $\Delta^{17}\text{O}(\text{O}_3)_{\text{bulk}}$ matches remarkably well the February-March
 495 measurements reported by Vicars and Savarino (2014).

496 3.3 Interpretation of $\Delta^{17}\text{O}$ in atmospheric nitrate

497 Over the two sampling periods, $\Delta^{17}\text{O}(\text{NO}_3^-)$ varies significantly (from 18.3 ‰ to 28.1 ‰), with a weighted mean of $(22.5 \pm$
 498 $3.1) \text{‰}$. While $\Delta^{17}\text{O}(\text{NO}_2)$ values are relatively similar during the two sampling periods, $\Delta^{17}\text{O}(\text{NO}_3^-)$ values are
 499 systematically higher during SP 2 than during SP 1, except during the 7:30–10:00 LT interval. $\Delta^{17}\text{O}(\text{NO}_3^-)$ in Chamonix is
 500 in the same range of most previous observations in urban environments (9–44 ‰; e.g., Kim et al., 2023; Wang et al., 2023;
 501 Fan et al., 2023; Zhang et al., 2022b; Lim et al., 2022; Li et al., 2022b), but lower than most values measured during the cold

502 season which are typically >25 ‰. Unlike $\Delta^{17}\text{O}(\text{NO}_2)$, daytime and nighttime $\Delta^{17}\text{O}(\text{NO}_3^-)$ values at our site are not
503 significantly different (p -value > 0.05, $n = 14$). Similarly, from 12 h resolved sampling in winter Beijing, He et al. (2018)
504 found no significant difference between daytime and nocturnal $\Delta^{17}\text{O}(\text{NO}_3^-)$ and suggest that each sample reflects NO_3^-
505 produced during both the day and night. From high-time-resolved (3 h) aerosol sampling in winter Beijing, Zhang et al.
506 (2022b) reported $\Delta^{17}\text{O}(\text{NO}_3^-)$ values between 23.4 ‰ to 39.3 ‰, with higher values observed at night ((31.0 ± 2.6) ‰) than
507 during the day ((29.3 ± 3.0) ‰). This diurnal behaviour of $\Delta^{17}\text{O}(\text{NO}_3^-)$ was attributed to the changes in the branching ratio of
508 nocturnal and photochemical reactions on NO_3^- formation. In Chamonix, the range of $\Delta^{17}\text{O}(\text{NO}_3^-)$ values are very different
509 from Zhang et al., (2022b) observations, with consistently lower values and a distinct diurnal tendency. However, in the
510 cases of $\Delta^{17}\text{O}(\text{NO}_3^-)$ measurements at sub-daily temporal scale, the atmospheric lifetime of NO_x and NO_3^- is critical for
511 comparing $\Delta^{17}\text{O}(\text{NO}_3^-)$ records from one site to another. Pollutant levels and atmospheric conditions between Chamonix and
512 Beijing are very different, notably in winter when Asian urban areas can experience severe haze pollution episodes with
513 NO_3^- mass concentration exceeding $70 \mu\text{g m}^{-3}$, which is over 10 times higher than in Chamonix (Lim et al., 2022; He et al.,
514 2018; Zhang et al., 2022b). In such conditions, PM can reach several hundreds of $\mu\text{g m}^{-3}$ for several days, which can
515 significantly impact atmospheric processes involved in the formation of secondary species. Aside from the intrusion of
516 Saharan dust during SP 2, the pollutant level in Chamonix is indicative of a moderately polluted region, with significant
517 diurnal variations.

518 3.3.1 Steady state evaluation of $\Delta^{17}\text{O}(\text{NO}_3^-)$

519 To investigate the factors influencing the variability of $\Delta^{17}\text{O}(\text{NO}_3^-)$ at our site, one compare observed $\Delta^{17}\text{O}(\text{NO}_3^-)$ with
520 estimated values of $\Delta^{17}\text{O}(\text{NO}_3^-)$ derived from $\Delta^{17}\text{O}$ mass balance and observed $\Delta^{17}\text{O}(\text{NO}_2)$, assuming the OH and N_2O_5
521 pathways dominate the formation of NO_3^- at our site. Therefore, calculated $\Delta^{17}\text{O}(\text{NO}_3^-)$ reflect the theoretical $\Delta^{17}\text{O}$ transfer
522 during the oxidation of NO_2 to NO_3^- at our site through the dominant chemical process during the day (i.e. OH pathway) and
523 at night (i.e. N_2O_5 pathway).

524

525 As presented, during the day, we consider that the conversion of NO_2 into NO_3^- is predominantly influenced by
526 Reaction (R5) (OH pathway). Hence, the theoretical corresponding ^{17}O -excess transfer to NO_3^- is estimated using Eq. (6)
527 and observed $\Delta^{17}\text{O}(\text{NO}_2)$ between 7:30 and 18:00 LT ($n = 3$ per sampling period). Then, in order to estimate a daytime
528 average value of $\Delta^{17}\text{O}(\text{NO}_3^-)$ which is representative of the potential for the formation of NO_3^- from surface NO_2 by the OH
529 pathway, each calculated $\Delta^{17}\text{O}(\text{NO}_3^-)$ is weighted by the product $[\text{NO}_2] \times J_{\text{NO}_2}$ (the diurnal variability of the OH mixing ratio
530 is assumed to follow the diurnal J_{NO_2} variation; Liu et al., 2021). Finally, an overall mean daytime $\Delta^{17}\text{O}(\text{NO}_3^-)$ for SP 1 and
531 SP 2 is estimated by taking the sum of the weighted calculated values ($=\Delta^{17}\text{O}_{\text{calc}}(\text{NO}_3^-)$). The same approach is used during
532 the night, assuming that the conversion of NO_2 into NO_3^- is dominated by Reactions (R6)–(R8) (N_2O_5 pathway). Eq. (7) and

533 observed $\Delta^{17}\text{O}(\text{NO}_2)$ between 18:00 and 7:30 LT ($n = 3$ per sampling day) are used to estimate $\Delta^{17}\text{O}(\text{NO}_3^-)$. Each calculated
534 $\Delta^{17}\text{O}(\text{NO}_3^-)$ is weighted by the product $[\text{NO}_2] \times [\text{O}_3]$ (i.e., NO_3^- production rate) and summed to estimate a mean nighttime
535 $\Delta^{17}\text{O}(\text{NO}_3^-)$ for SP 1 and SP 2. The ^{17}O -excess transferred from O_3 to NO_2 during Reaction (R6) ($\Delta^{17}\text{O}_{\text{NO}_2+\text{O}_3}(\text{NO}_3^-)$) is
536 fixed at 44.7 ‰. This value is set accordingly to the transfer function reported by Berhanu et al. (2012) whereby
537 $\Delta^{17}\text{O}_{\text{NO}_2+\text{O}_3}(\text{NO}_3^-) = (1.23 \pm 0.19) \times \Delta^{17}\text{O}(\text{O}_3)_{\text{bulk}} + (9.02 \pm 0.99)$ and $\Delta^{17}\text{O}(\text{O}_3)_{\text{bulk}} = 29.0$ ‰ (see Section 2.4.1). We
538 compare hereafter $\Delta^{17}\text{O}_{\text{calc}}(\text{NO}_3^-)$ with the weighted day and night averages of observed $\Delta^{17}\text{O}(\text{NO}_3^-)$ at our site. During the
539 day, $\Delta^{17}\text{O}_{\text{calc}}(\text{NO}_3^-)$ is compared with $\Delta^{17}\text{O}(\text{NO}_3^-)$ observations averaged between 7:30 and 18:30 LT ($n = 3$). At night,
540 $\Delta^{17}\text{O}_{\text{calc}}(\text{NO}_3^-)$ is compared with $\Delta^{17}\text{O}(\text{NO}_3^-)$ observations averaged between 18:30 to 7:30 LT.

541

542 At night during SP 1, observed $\Delta^{17}\text{O}(\text{NO}_3^-)$ and $\Delta^{17}\text{O}_{\text{calc}}(\text{NO}_3^-)$ are in good agreement ($\Delta^{17}\text{O}_{\text{calc}}(\text{NO}_3^-) - \Delta^{17}\text{O}(\text{NO}_3^-) =$
543 $\Delta^{17}(\text{NO}_3^-_{\text{calc}} - \text{NO}_3^-_{\text{obs}}) = 0.9$ ‰), suggesting a local and rapid (< 12 h) conversion of NO_2 into NO_3^- via the N_2O_5 pathway.
544 During the day, observed $\Delta^{17}\text{O}(\text{NO}_3^-)$ is 0.5 ‰ higher than $\Delta^{17}\text{O}_{\text{calc}}(\text{NO}_3^-)$, also suggesting that NO_3^- is formed locally
545 during the day for oxidation of surface NO_2 through the OH pathway. Small differences between observed and calculated
546 $\Delta^{17}\text{O}$ of NO_3^- during the day/night could be explained by the presence of NO_3^- residues formed during the previous
547 night/day, which are not considered in the calculations since they do not account for NO_3^- lifetime. In contrast to SP 1,
548 $\Delta^{17}\text{O}_{\text{calc}}(\text{NO}_3^-)$ during SP 2 is significantly lower than the mean observed $\Delta^{17}\text{O}(\text{NO}_3^-)$, particularly during the day with a
549 $\Delta^{17}(\text{NO}_3^-_{\text{calc}} - \text{NO}_3^-_{\text{obs}})$ of -6.4 ‰. The significant gap between observed and calculated $\Delta^{17}\text{O}(\text{NO}_3^-)$ suggests a different
550 origin and/or formation process of NO_3^- during SP 2 compared to SP 1. Although less important than during the day,
551 $\Delta^{17}\text{O}_{\text{calc}}(\text{NO}_3^-)$ values for SP 2 at night is lower by 2.2 ‰ to the observed value. This small shift can be explained by
552 residuals of enriched daytime NO_3^- . It is important to point out that, although the NO_2 sample collected on Feb 24 between
553 13:30 and 16:30 LT presents an important blank (ca. 14 ‰), ambient NO_2 is low during the sampling period (mean of $(4.5 \pm$
554 $1.8)$ nmol mol $^{-1}$). Therefore, as each $\Delta^{17}\text{O}$ value used to estimate $\Delta^{17}\text{O}_{\text{calc}}(\text{NO}_3^-)$ is weighted by the mean ambient NO_2
555 mixing ratio over the sampling period, the uncertainty related to this blank has little influence on the daily average of
556 $\Delta^{17}\text{O}_{\text{calc}}(\text{NO}_3^-)$. Given the low $\Delta^{17}(\text{NO}_3^-_{\text{calc}} - \text{NO}_3^-_{\text{obs}})$ during SP 1, observed $\Delta^{17}\text{O}(\text{NO}_3^-)$ can be explained by the local and
557 rapid (< 12 h) oxidation of NO_2 , dominated by the OH and N_2O_5 pathway during the day and night, respectively. However,
558 in contrast to SP 1, the ^{17}O -excess measured in NO_3^- during the day of SP 2 cannot be fully constrained by the oxidation of
559 surface NO_2 through the OH pathway, suggesting that the formation mechanisms of NO_3^- are different between SP 1 and SP
560 2 and/or the presence of NO_3^- not formed locally during SP 2. Below we examine the changes in the sub-daily dynamics of
561 $\Delta^{17}\text{O}(\text{NO}_3^-)$ between SP 1 and SP 2 in light of atmospheric observations.

562

		$\Delta^{17}\text{O}(\text{NO}_2)$ /‰	$\Delta^{17}\text{O}(\text{NO}_3^-)$ /‰	$\Delta^{17}\text{O}_{\text{calc}}(\text{NO}_3^-)$ /‰	$\Delta^{17}(\text{NO}_3^-_{\text{calc}} - \text{NO}_3^-_{\text{obs}})$
Daytime (7:30-18:00)	SP 1	30.0 ± 7.3	23.0 ± 3.1	22.5 ± 4.6	-0.5
	SP 2	26.1 ± 6.9	23.9 ± 3.8	17.5 ± 4.6	-6.4
Nighttime (18:00-7:30)	SP 1	21.2 ± 1.1	20.5 ± 1.1	21.4 ± 0.7	0.9
	SP 2	20.8 ± 1.0	23.2 ± 1.0	21.0 ± 0.6	-2.2

563 **Table 2.** Mean observed $\Delta^{17}\text{O}$ data of NO_2 ($\Delta^{17}\text{O}(\text{NO}_2)$) and NO_3^- ($\Delta^{17}\text{O}(\text{NO}_3^-)$) in Chamonix, and mean calculated $\Delta^{17}\text{O}$ of NO_3^-
564 ($\Delta^{17}\text{O}_{\text{calc}}(\text{NO}_3^-)$) using Eqs. (6) and (7) at day and night, respectively, constrained with observed $\Delta^{17}\text{O}(\text{NO}_2)$. Day and night calculated
565 values were weighted by $[\text{NO}_2] \times J_{\text{NO}_2}$ and $[\text{NO}_2] \times [\text{O}_3]$, respectively

566

567 3.3.2 $\Delta^{17}(\text{NO}_3^-)$ sub-daily dynamics

568 Between 7:30–10:30 LT, $\Delta^{17}\text{O}(\text{NO}_3^-)$ is very similar during SP 1 (18.3 ‰) and SP 2 (18.6 ‰). Nonetheless, on the
569 following sampling time step (i.e., between 10:30–13:30 LT), $\Delta^{17}\text{O}(\text{NO}_3^-)$ is significantly different between SP 1 (21.5 ‰)
570 and SP 2 (24.7 ‰). Intriguingly, between 7:30–13:30 LT, $\Delta^{17}\text{O}(\text{NO}_2)$ during SP 2 (26.9 ‰) is lower compared to SP 1 (32.8
571 ‰). As a consequence, if one consider that NO_3^- is formed from the oxidation of local NO_2 through identical pathways
572 during SP 1 and SP 2, observed $\Delta^{17}\text{O}(\text{NO}_3^-)$ should be lower during SP 2 than during SP 1. Therefore, the more pronounced
573 increase of observed $\Delta^{17}\text{O}(\text{NO}_3^-)$ during the 10:30–12:30 LT interval of SP 2 suggests a different origin and/or formation
574 channel of NO_3^- , as mentioned previously. One more piece of evidence is that, during this period of time, PM_{10} and NO_3^-
575 levels increase significantly during SP 2, alongside the disruption of the inversion layer (depicted in Figure 1). It can be
576 inferred that this rise in PM_{10} is mostly due to the presence of Saharan dust. The simultaneous increase of NO_3^- and of
577 $\Delta^{17}\text{O}(\text{NO}_3^-)$ corroborates the hypothesis that this NO_3^- was not formed from the oxidation of ambient NO_2 . Furthermore,
578 such an increase in $\Delta^{17}\text{O}(\text{NO}_3^-)$ can only be supported by the oxidation of NO_2 through the N_2O_5 pathway, which is not
579 expected to be important during the day due to the rapid photolysis of NO_3 and its titration by NO (Brown and Stutz, 2012).

580

581 Interestingly, aerosol samplings conducted at various heights (8 m, 120 m, and 260 m above ground level) in Beijing,
582 China, revealed a positive vertical gradient of $\Delta^{17}\text{O}(\text{NO}_3^-)$ in winter, from on average 29 ‰ to 33 ‰ (Fan et al., 2022). In
583 summer, the $\Delta^{17}\text{O}(\text{NO}_3^-)$ values at the three altitudes were very similar. This increase of $\Delta^{17}\text{O}(\text{NO}_3^-)$ with altitude in winter
584 was believed to result from a stratification of NO_2 to NO_3^- oxidation processes due to low vertical mixing and elevated
585 surface NO_x emissions. However, the authors did not consider the potential variability of $\Delta^{17}\text{O}(\text{NO}_2)$ with altitude, which can
586 be substantial in urban areas at night as low $\Delta^{17}\text{O}(\text{NO}_2)$ results from surface NO oxidation. For our study, we propose an
587 alternative interpretation of the vertical variability of $\Delta^{17}\text{O}(\text{NO}_3^-)$, where $\Delta^{17}\text{O}(\text{NO}_2)$ is considered as the main driver. During
588 the formation of the nocturnal boundary layer, NO_2 formed during the day can be trapped above the surface layer in the

589 nocturnal residual layer (NRL). This NO_2 has a high $\Delta^{17}\text{O}$ because it was formed during the previous daytime hours under
590 the ISS framework (Eq. (3)). Throughout the night, this highly enriched NO_2 (ca. 37 ‰ which is the average of the
591 maximum $\Delta^{17}\text{O}(\text{NO}_2)$ during SP 1 and SP 2) can be converted to NO_3^- via the N_2O_5 pathway, hence leading to a substantial
592 $\Delta^{17}\text{O}$ transfer to NO_3^- at around 32 ‰, which is in the range of $\Delta^{17}\text{O}(\text{NO}_3^-)$ observed by Fan et al. (2022) in winter. In the
593 meantime, NO emitted at the surface during the night can be converted to NO_2 by O_3 , with a $\Delta^{17}\text{O}$ transfer of ca. 20 ‰ (Eq.
594 (5) with $x = 0$). This low enriched NO_2 can be further oxidised to NO_3^- by the N_2O_5 pathway which results in a $\Delta^{17}\text{O}$ transfer
595 at around 21 ‰. This NO_2 with a low $\Delta^{17}\text{O}$ is very likely to be formed only at the surface during the night in areas
596 experiencing important NO_x emissions (Michalski et al., 2014). Furthermore, surface NO_2 with low $\Delta^{17}\text{O}$ is not expected to
597 be transported aloft as it is formed in the surface inversion layer during the night. Therefore, NO_3^- formed in the NRL during
598 winter nights may be more enriched than the NO_3^- formed concurrently at the surface, regardless of the NO_2 oxidation
599 process involved. When the inversion layer breaks during the following day, the NO_3^- that was formed in the NRL during
600 the night is mixed with the NO_3^- formed at the surface, resulting in an increase in the overall surface $\Delta^{17}\text{O}$. In this scenario,
601 the presence of the Saharan dust during SP 2 may have increased the NO_3^- loading aloft by promoting heterogeneous
602 processes on aerosol surfaces in the vicinity of Chamonix. Hence, NO_2 stratification at night could explain the observed
603 increase in $\Delta^{17}\text{O}$ of NO_3^- at the surface following the collapse of the nocturnal inversion layer. However, we cannot
604 determine whether the enriched NO_3^- were formed in the vicinity of Chamonix and/or transported to our site by Saharan
605 dust.

606

607 Although the exact nature of the high ^{17}O -excess measured in NO_3^- during SP 2 remains unclear, boundary layer
608 dynamics is thought to play a significant role in the variability of $\Delta^{17}\text{O}(\text{NO}_3^-)$ at the surface due to the stratification of NO_2 .
609 Therefore, a wider consideration of such factors should be explored to avoid possible over-interpretation of $\Delta^{17}\text{O}(\text{NO}_3^-)$
610 variabilities at the surface, especially in urban areas experiencing significant boundary layer dynamics in winter and high
611 surface emissions of NO_x at night. Measuring $\Delta^{17}\text{O}(\text{NO}_2)$ at various altitudes could provide better insights on the vertical
612 dynamics of $\Delta^{17}\text{O}(\text{NO}_3^-)$, and subsequently quantitative information on NO_3^- production processes.

613

614 3.4 Nitrogen isotopic compositions

615 3.4.1 N fractionation effects in the NO_x cycle

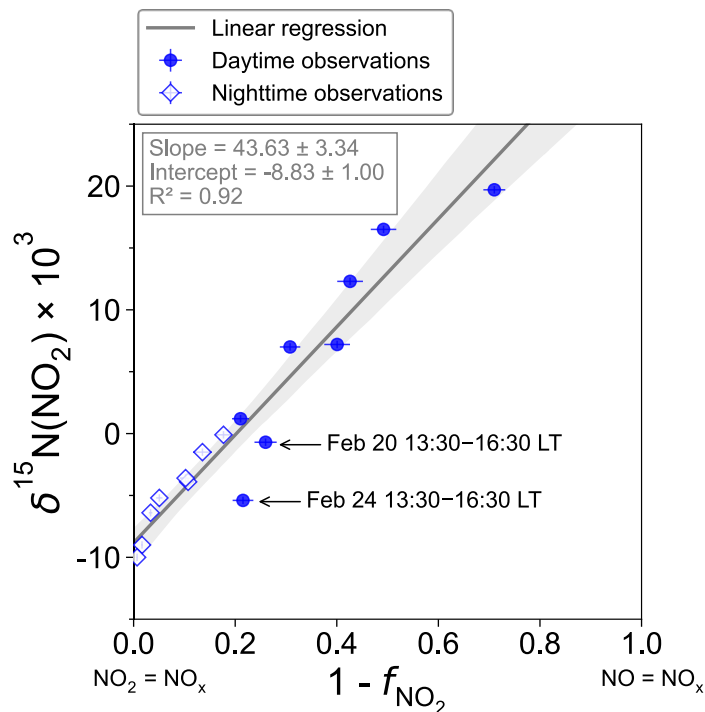
616 Over the two sampling periods, $\delta^{15}\text{N}(\text{NO}_2)$ shows substantial diurnal variability (from -10.0 ‰ to 19.7 ‰, $n = 16$) with a
617 weighted mean of (4.0 ± 9.1) ‰. In contrast, Albertin et al. (2021) reported a weak diurnal fluctuation of $\delta^{15}\text{N}(\text{NO}_2)$ in
618 spring in Grenoble, in a narrow range from about -12 ‰ to -10 ‰. In summer in an urban/suburban location, Walters et al.
619 (2018) also observed a wide range of $\delta^{15}\text{N}(\text{NO}_2)$ values, however, unlike our study, these are almost consistently negative

620 (from -31.4 ‰ to 0.4 ‰) with an overall mean at (-11.4 ± 6.9) ‰. As shown in Eq. (8), fluctuations in $\delta^{15}\text{N}(\text{NO}_2)$ reflect
621 changes in NO_x emission sources and/or N fractionation effects, these latter being weighted by $1 - f_{\text{NO}_2}$ i.e., the more NO_x is
622 under the form of NO , the greater the N fractionation effects (see Section 2.4). Hence, in the previous works of Albertin et
623 al. (2021) and Walters et al. (2018), due to high f_{NO_2} (> 0.7), isotope effects were small (< 2.7 ‰) and $\delta^{15}\text{N}(\text{NO}_2)$ was mostly
624 driven by changing contribution of NO_x emission sources. At our site, f_{NO_2} shows a wider range, from 0.3 to 1.0, suggesting
625 significant N isotopic fractionation effects, with minimum and maximum contributions corresponding to the highest and
626 lowest observed value of $\delta^{15}\text{N}(\text{NO}_2)$, respectively. This pronounced seasonal behaviour of N isotope fractionation effects
627 within the NO_x cycle has previously been outlined in the seminal study of Freyer et al. (1993). Overall, compared with
628 summer, lower f_{NO_2} during winter months due to lower O_3 concentrations and higher NO_x emissions favour EIE between NO
629 and NO_2 , which also has a higher fractionation factor due to the lower temperatures (see Appendix D: Equilibrium N
630 fractionation factors). Besides, this seasonal fluctuation of f_{NO_2} can be expected to be observed on smaller time scales,
631 typically on the diurnal scale in urban areas where NO is generally fully oxidised into NO_2 at night due to a lower NO_x
632 emission rate resulting in higher f_{NO_2} at night than during the day, as observed at our sampling (Figure 2).

633

634 Figure 3 shows the linear dependence of $\delta^{15}\text{N}(\text{NO}_2)$ on $(1 - f_{\text{NO}_2})$ over the two sampling periods, indicating the
635 significant influence of atmospheric processes that alter the N isotopic distribution during the conversion of NO_x into NO_2 .
636 The linear regression gives a slope and an intercept of about (43.6 ± 3.3) ‰ and (-8.8 ± 1.0) ‰, respectively. According to
637 Eqs. (10) and (11), the linearity between daytime (07:30–18:00 LT) and nighttime (18:00–07:30 LT) values suggests that
638 EIE dominates the N fractionation processes between NO_x and NO_2 . The influence of LCIE during the day could explain the
639 greater variability around the linear fit in the daytime observations.

640



641
642

643 **Figure 3.** Correlation plot of $\delta^{15}\text{N}$ of atmospheric NO_2 vs. $(1 - f_{\text{NO}_2})$ from observations in Chamonix in February 2021. f_{NO_2} are averaged
644 over the collection period of each NO_2 sample. The grey shade is the 95 % confidence interval. White diamonds and blue dots represent
645 the nighttime (18:00–07:30 LT) and daytime (07:30–18:00 LT) observations, respectively. The linear regression is plotted over the
646 nighttime and daytime observations.

647 The relative importance of EIE and LCIE in the N fractionation between emitted NO_x and NO_2 is assessed by
648 calculating the A^* factor during the day (7:30–18:00 LT; A^*_{day}) and night (18:00–7:30 LT; A^*_{night}) (Table 3). A^*_{day} and A^*_{night}
649 expressions are given in Section 2.4.2. Overall, during NO_2 sampling intervals, the A^* values are small (mean \pm one standard
650 deviation: 0.21 ± 0.51) and reflect an EIE-dominated regime with high NO_x (Li et al., 2020). It is interesting to note that the
651 highest A^* values are observed between 13:30 and 16:30 LT, and correspond to the two data points in Figure 3 that lie
652 outside the 95 % confidence interval of the regression line. These results suggest that EIE is the dominant N fractionation
653 processes between NO_x and NO_2 during both day and night ($A^* < 0.46$), with the exception of mid-afternoon when LCIE
654 competes with EIE ($A^* > 0.46$).

655

656 To quantify the overall N fractionation effect (F_N) between NO_x and NO_2 , we dissociate the two samples collected
657 between 13:30 and 16:30 LT into a different group (Group #1 = GP 1) from the other samples (Group #2 = GP 2). F_N of GP
658 1 and GP 2 is calculated using Eq. (10) (which combines LCIE and EIE regimes) and Eq. (11) (which considers only the EIE
659 regime), respectively. Calculated F_N are reported in Table 3 and data used for calculations can be found in Section 2.4.2 and

660 in the Supplement. Calculated F_N is significantly different between GP 1 and GP 2, with a mean of 16.4 ‰ and 42.3 ‰,
661 respectively. The close match between the calculated average F_N of GP 2 and the observed F_N ((43.6 ± 3.3) ‰; slope of the
662 regression line in Figure 3) provides strong evidence for the reliability of Eq. (11), as well as the expression of $\alpha_{\text{EIE}(\text{NO}_2/\text{NO})}$
663 used therein, to accurately describe the N fractionation between NO_x emissions and NO_2 at our site, and hence, to describe
664 most of the variability of $\delta^{15}\text{N}(\text{NO}_2)$ measurements. This result holds significant importance in confirming the theoretical N
665 isotopic fractionation framework used in prior research studies. It is also important to stress the influence of LCIE effects for
666 GP 1, highlighting the high dependency of $\delta^{15}\text{N}(\text{NO}_2)$ to local environmental conditions. According to the A^* factor, a
667 greater influence of LCIE in mid-afternoon could have contributed to the outlying of the two samples collected between
668 13:30 and 16:30 LT (GP 1). However, as mentioned above, the sample collected on Feb 24 between 13:30 and 16:30 LT has
669 a significant blank. Therefore, it cannot be confirmed with certainty that the reason this sample falls outside the 95 %
670 confidence interval of the regression line is solely due to LCIE. Nevertheless, the overall conclusion that EIE dominates the
671 variability of $\delta^{15}\text{N}(\text{NO}_2)$ at our site is not affected by this uncertainty.

672

673 The $\delta^{15}\text{N}$ shift in NO_2 relative to emitted NO_x ($\Delta^{15}(\text{NO}_2 - \text{NO}_x)$) is calculated for individual NO_2 sample using the mean
674 ambient temperature during each sampling period. The mean atmospheric $\delta^{15}\text{N}$ of NO_x ($\delta^{15}\text{N}(\text{NO}_x)$) is then estimated by
675 subtracting the $\Delta^{15}(\text{NO}_2 - \text{NO}_x)$ value from the observed $\delta^{15}\text{N}(\text{NO}_2)$ value. $\Delta^{15}(\text{NO}_2 - \text{NO}_x)$ and $\delta^{15}\text{N}(\text{NO}_x)$ estimates are
676 reported in Table 3. $\Delta^{15}(\text{NO}_2 - \text{NO}_x)$ varies greatly over the two sampling periods (from 0.7 ‰ to 30.7 ‰) with a mean value
677 of ca. 9 ‰ (mean of GP #1 and GP #2). $\delta^{15}\text{N}(\text{NO}_x)$ show much less variability with an overall mean at (-7.8 ± 1.9) ‰ (mean
678 of GP #1 and GP #2), in very good agreement with the value derived from the regression relationship (-8.8 ‰; intercept of
679 the regression line in Figure 3). Therefore, there appears that there is little variation in NO_x emission sources at our site, and
680 the wide variability in $\delta^{15}\text{N}(\text{NO}_2)$ is mainly driven by important equilibrium post-emission isotopic effects.

681

Sampling interval (start – end)	$A^{*(1)}$	$F_N^{(2)}$	f_{NO_2}	$\Delta^{15}(NO_2 - NO_x)^{(3)}$ /‰	$\delta^{15}N(NO_x)$ /‰
GP #1					
20/02 13:30 – 20/02 16:30	0.46 ± 0.08	25.00 ± 2.27	0.74 ± 0.02	6.5 ± 0.9	-7.2 ± 0.9
24/02 13:30 – 24/02 16:30	2.09 ± 0.39	6.90 ± 1.97	0.78 ± 0.02	1.5 ± 0.4	-6.9 ± 0.6
<i>Mean</i>	<i>1.27</i>	<i>16.39</i>	<i>0.76</i>	<i>4.1</i>	<i>-7.1</i>
<i>Std dev</i>	<i>1.14</i>	<i>12.58</i>	<i>0.03</i>	<i>3.5</i>	<i>0.2</i>
GP #2					
19/02 21:00 – 20/02 00:30	0.03 ± 0.01	43.06 ± 0.17	0.97 ± 0.01	1.4 ± 0.1	-7.8 ± 0.3
20/02 00:30 – 20/02 04:30	0.07 ± 0.01	43.51 ± 0.18	0.98 ± 0.01	0.7 ± 0.1	-9.7 ± 0.3
20/02 04:30 – 20/02 07:30	0.02 ± 0.01	43.78 ± 0.22	0.89 ± 0.01	4.7 ± 0.4	-8.6 ± 0.5
20/02 07:30 – 20/02 10:30	0.05 ± 0.01	43.92 ± 0.18	0.60 ± 0.02	17.6 ± 1.0	-10.4 ± 1.1
20/02 10:30 – 20/02 13:30	0.10 ± 0.02	43.06 ± 0.18	0.57 ± 0.02	18.4 ± 1.0	-6.1 ± 1.0
20/02 16:30 – 20/02 18:00	0.03 ± 0.01	39.97 ± 0.18	0.69 ± 0.02	12.3 ± 0.8	-5.3 ± 0.8
20/02 18:00 – 20/02 21:00	0.01 ± 0.01	41.75 ± 0.19	0.90 ± 0.01	4.3 ± 0.5	-7.9 ± 0.6
24/02 07:30 – 24/02 10:30	0.01 ± 0.01	43.21 ± 0.18	0.29 ± 0.02	30.7 ± 0.9	-11.9 ± 0.9
24/02 10:30 – 24/02 13:30	0.07 ± 0.01	41.95 ± 0.18	0.51 ± 0.02	20.6 ± 1.0	-4.1 ± 1.1
24/02 16:30 – 24/02 18:00	0.16 ± 0.03	39.80 ± 0.16	0.79 ± 0.02	8.4 ± 0.6	-7.2 ± 0.7
24/02 18:00 – 24/02 21:00	0.01 ± 0.01	40.88 ± 0.18	0.82 ± 0.02	7.2 ± 0.6	-7.3 ± 0.6
24/02 21:00 – 25/02 00:00	0.03 ± 0.02	42.20 ± 0.19	0.95 ± 0.01	2.1 ± 0.3	-7.3 ± 0.4
25/02 00:00 – 25/02 04:00	0.19 ± 0.03	42.48 ± 0.18	0.99 ± 0.01	0.3 ± 0.1	-10.3 ± 0.3
25/02 04:00 – 25/02 07:30	0.09 ± 0.01	42.69 ± 0.17	0.86 ± 0.02	5.8 ± 1.0	-7.3 ± 1.0
<i>Mean</i>	<i>0.06</i>	<i>42.31</i>	<i>0.77</i>	<i>9.6</i>	<i>-7.9</i>
<i>Std dev</i>	<i>0.06</i>	<i>1.32</i>	<i>0.21</i>	<i>9.1</i>	<i>2.0</i>

(¹) Calculated from A^{*}_{day} between 7:30–18:00 LT and from A^{*}_{night} between 18:00–07:30 LT (A^{*}_{day} and A^{*}_{night} expressions are given in Section 2.4.2).

(²) Calculated from Eq. (10) for GP 1 and from Eq. (11) for GP 2

(³) Calculated from Eq. (9)

682 **Table 3.** Summary table of data used to estimate the N isotopic fractionation between NO_x emissions and NO_2 at our site ($\Delta^{15}(NO_2 -$
683 $NO_x)$) and derive NO_x emissions $\delta^{15}N$ -fingerprint $\delta^{15}N(NO_x)$. The data reported are the mean values for each NO_2 sampling period (mean
684 value ± absolute uncertainty).

685 3.4.2 NO_x emission sources derived from $\delta^{15}N(NO_2)$

686 To identify the main source of NO_x that contributes to the calculated $\delta^{15}N(NO_x)$ values at our site, Figure 4 displays the
687 temporal variation of $\delta^{15}N(NO_x)$ obtained from individual NO_2 samples (dashed horizontal line) and the $\delta^{15}N$ range for
688 different NO_x emission sources (coloured bands) such as for coal combustion ((19.5 ± 2.3) ‰ for power plant with selective
689 catalytic reduction technology; Felix et al., 2012; Elliott et al., 2019), fossil gas combustion ((-16.5 ± 1.7) ‰; Walters et al.,
690 2015), and fertilised soils ((-33.8 ± 12.2) ‰; Miller et al., 2018). $\delta^{15}N$ of NO_x released during biomass combustion is
691 primarily driven by the $\delta^{15}N$ of the biomass burnt (Fibiger and Hastings, 2016). We estimate an average $\delta^{15}N$ of biomass
692 combustion NO_x at (-0.1 ± 1.3) ‰, using the empirical relationship of Chai et al. (2019) (which was derived from

693 combustions of several North American wood species) and an average $\delta^{15}\text{N}$ of biomass at $(-2.8 \pm 2.0) \text{‰}$ representative of
694 temperate forests (Martinelli et al., 1999). Regarding road traffic emissions, we have to stress that $\delta^{15}\text{N}$ values reported in the
695 literature are rather variable mainly because N fractionations during the process of NO_x production can vary depending on
696 the type of fuel used, the type of vehicle, the presence of an emission control system, and the time of commuting (Ammann
697 et al., 1999; Felix and Elliott, 2014; Heaton, 1990; Miller et al., 2017; Walters et al., 2015b; Zong et al., 2020, 2017). We use
698 here the mean vehicle-emitted $\delta^{15}\text{N}(\text{NO}_x)$ value given by Song et al. (2022) at $(-7.1 \pm 4.1) \text{‰}$, calculated from 181
699 measurements reported in the literature.

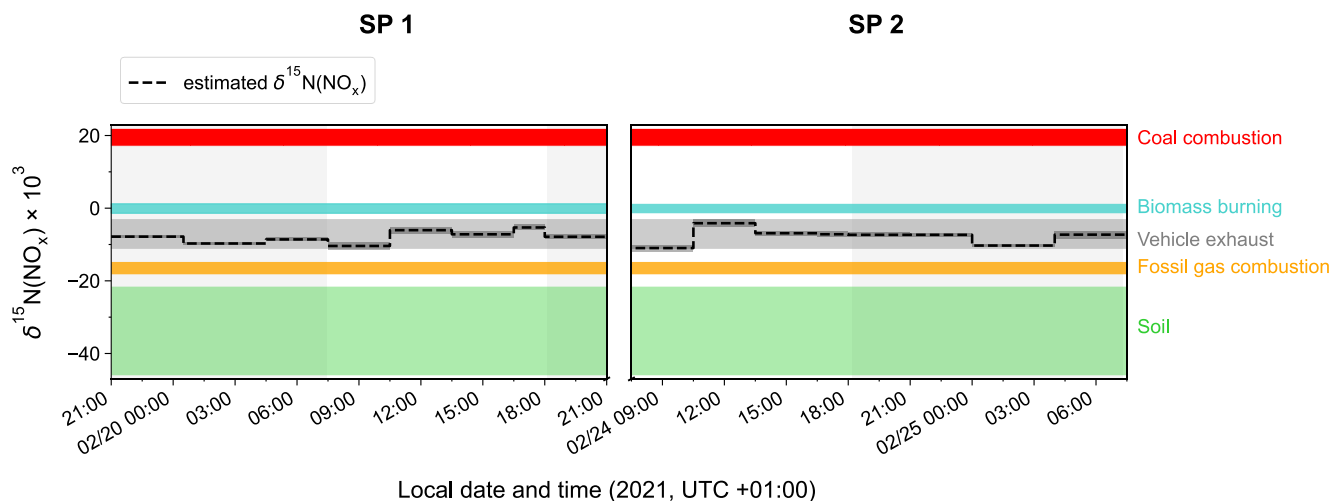
700

701 As previously noted, the values of estimated $\delta^{15}\text{N}(\text{NO}_x)$ show much less variability than $\delta^{15}\text{N}(\text{NO}_2)$, with no significant
702 differences observed between daytime and nighttime values. The values of $\delta^{15}\text{N}(\text{NO}_x)$ range from -11.0‰ to -4.1‰ , and
703 despite the associated uncertainty, they are consistent with the $\delta^{15}\text{N}$ range of NO_x emissions from vehicle exhaust. The two
704 sampling periods show similar $\delta^{15}\text{N}(\text{NO}_x)$ values with a slight diel variability. The estimated small variation in $\delta^{15}\text{N}(\text{NO}_x)$
705 throughout the day can be attributed to the temporal changes in the $\delta^{15}\text{N}$ signature of mobile NO_x sources. It has been shown
706 that NO_x emitted by cold engines has a lower $\delta^{15}\text{N}$ signature compared to NO_x emitted from warm engines (Walters et al.,
707 2015b). Hence, the early morning drop in $\delta^{15}\text{N}(\text{NO}_x)$ could be attributed to the influence of NO_x emitted from cold engines.
708 As the day progresses, the time of commuting increases and therefore $\delta^{15}\text{N}(\text{NO}_x)$ tends to be less negative. Conversely,
709 during the night, the slow $\delta^{15}\text{N}(\text{NO}_x)$ decline could be due to the replacement of NO_x from vehicle exhaust by NO_x emitted
710 by fossil gas combustion, which is commonly used in Chamonix for home heating. Although biomass burning used for home
711 heating would also tend to increase $\delta^{15}\text{N}(\text{NO}_x)$ during the day, it is unlikely to contribute more during the day than at night.

712

713 According to local NO_x emission inventories (Atmo-Auvergne-Rhône-Alpes, 2018; ORCAE, 2022), road transport is
714 responsible of 64 % of NO_x emissions, ahead of heating oil and fossil gas combustion. Despite the consistency between our
715 results and existing inventories, the significant variability in the $\delta^{15}\text{N}$ signature of NO_x emissions from vehicle exhaust
716 precludes a reliable quantitative source apportionment of NO_x emissions from our estimated $\delta^{15}\text{N}(\text{NO}_x)$. Furthermore, the
717 lack of information on the exact $\delta^{15}\text{N}$ signature of NO_x emitted from heating-oil combustion could also contribute to the
718 potential bias of the emission source apportionment.

719



720

721 **Figure 4.** Time evolution of $\delta^{15}\text{N}(\text{NO}_x)$ (black dashed line) estimated from $\delta^{15}\text{N}(\text{NO}_2)$ observations in Chamonix after correction of N
 722 fractionation effects (length of horizontal line = sampling period, black shaded area = overall calculation error bar). Coloured shaded areas
 723 represent the standard deviation of the mean $\delta^{15}\text{N}$ value of individual NO_x emission source (coal combustion in red, biomass burning in
 724 blue, vehicle exhaust in grey, fossil gas in orange, and soil emissions in green). Grey backdrop shaded areas represent the nighttime (sunset
 725 to sunrise).

726 3.4.3 Interpretation of $\delta^{15}\text{N}(\text{NO}_3^-)$ observations

727 $\delta^{15}\text{N}(\text{NO}_3^-)$ also exhibits substantial variability during the day, ranging from -1.3‰ to 14.9‰ and from -4.2‰ to 9.7‰
 728 during SP 1 and SP 2, respectively. At night, $\delta^{15}\text{N}(\text{NO}_3^-)$ is less variable, with an overall mean of $(1.4 \pm 1.2)\text{‰}$ and $(-1.1 \pm$
 729 $0.4)\text{‰}$ during SP 1 and SP 2, respectively. $\delta^{15}\text{N}(\text{NO}_3^-)$ is within the range of observations reported in urban areas (He et al.,
 730 2020; Zhang et al., 2022a). A similar diurnal pattern was observed in samples collected during a cruise along the Californian
 731 coast in spring 2010 (Vicars et al., 2013), and isotopic exchanges between NO and NO_2 during the day were found to be the
 732 primary driver of the diel variability. In the previous section, we demonstrated that there is a significant ^{15}N partitioning
 733 between NO_x emissions and NO_2 , the latter being enriched in ^{15}N compared to NO_x emissions. Interestingly, important
 734 enrichments in ^{15}N are also observed in NO_3^- .

735

736 As described above, at night during SP 1 and SP 2, $\delta^{15}\text{N}(\text{NO}_2)$ is close to $\delta^{15}\text{N}(\text{NO}_x)$ due to small N fractionation
 737 effects. However, between 18:00–7:30 LT, NO_3^- is enriched in ^{15}N relative to NO_2 by $+6.3\text{‰}$ and $+1.4\text{‰}$ in average during
 738 SP 1 and SP 2, respectively (Table 4). If we assume that, at night, NO_3^- is formed mainly by the conversion of surface NO_2
 739 via the N_2O_5 pathway, then the difference between $\delta^{15}\text{N}(\text{NO}_3^-)$ and $\delta^{15}\text{N}(\text{NO}_2)$ ($\Delta^{15}\text{N}(\text{NO}_3^- - \text{NO}_2)$) should reflect the N
 740 enrichment factor associated to this oxidation process. It is likely that an isotopic equilibrium is established between NO_2 ,
 741 NO_3 , and N_2O_5 , hence affecting the partitioning of ^{15}N between NO_2 and NO_3^- produced at night (Walters and Michalski,
 742 2016). Neglecting KIE associated with the N_2O_5 pathway and using the expression of the EIE fractionation factor between
 743 N_2O_5 and NO_2 given by Walters and Michalski (2015) (Appendix D) constrained with the mean nighttime temperature at

744 our site, the isotopic composition of NO_3^- is expected be enriched in ^{15}N by about 29 ‰ compared to NO_2 . This estimated
 745 ^{15}N enrichment is about three times higher than the observed $\Delta^{15}(\text{NO}_3^- - \text{NO}_2)$ at our site. As daytime NO_3^- exhibits higher
 746 $\delta^{15}\text{N}$ values than during the night, it is not possible for daytime residuals at night to account for the lower than predicted
 747 fractionation effect between NO_2 and NO_3^- . These results highlight the importance of improving our understanding of the
 748 ^{15}N fractionation between NO_2 and NO_3^- associated with the N_2O_5 pathway. This could be achieved in an atmospheric
 749 simulation chamber that allows to reproduce individual processes in controlled conditions. The ^{15}N isotopic enrichment of
 750 NO_2 and NO_3^- collected from 7:30 to 18:00 LT shows a very contrasted distribution between SP 1 and SP 2, with a
 751 respective average $\Delta^{15}(\text{NO}_3^- - \text{NO}_2)$ of -0.4 ‰ and -10.0 ‰ (Table 4). Although subjected to significant uncertainties (Fan
 752 et al., 2019), the OH pathway is often associated to a KIE effect of -3 ‰ (Freyer, 1991), which is at odds with our
 753 observations. Similarly to the N_2O_5 pathway, there is an important need to better estimate the fractionation factor associated
 754 with the OH pathway.

755

756 There are significant differences in $\Delta^{15}(\text{NO}_3^- - \text{NO}_2)$ between SP 1 and SP 2, providing further evidence that NO_3^-
 757 collected during these two periods has undergone different formation processes and/or originate from different sources of
 758 NO_2 . In addition, possible fractionation associated with phase change between HNO_3 and $p\text{-NO}_3$ during transport of Saharan
 759 dust could influence the $\delta^{15}\text{N}$ of collected NO_3^- during SP 2. However, given the lack of knowledge about N fractionation
 760 factors between NO_2 and NO_3^- and our limited dataset, we cannot conclude whether the changes in the distribution of NO_3^-
 761 isotopes during SP 2 result from changes in the phase distribution of NO_3^- or in NO_2 oxidation processes.

762

		$\delta^{15}\text{N}(\text{NO}_2)$ /‰	$\delta^{15}\text{N}(\text{NO}_3^-)$ /‰	$\delta^{15}\text{N}(\text{NO}_x)$ /‰	$\delta^{15}\text{N}(\text{NO}_3^- - \text{NO}_2)$ /‰
Daytime (7:30-18:00)	SP 1	7.4 ± 4.7	7.0 ± 6.7	-9.9 ± 2.9	-0.4
	SP 2	14.0 ± 13.9	4.0 ± 6.4	-10.8 ± 2.1	-10.0
Nighttime (18:00-7:30)	SP 1	-5.1 ± 2.3	1.4 ± 1.2	-9.0 ± 0.8	6.3
	SP 2	-2.5 ± 4.2	-1.1 ± 0.4	-9.9 ± 1.9	1.4

763 **Table 4.** Mean observed $\delta^{15}\text{N}$ data of NO_2 ($\delta^{15}\text{N}(\text{NO}_2)$) and NO_3^- ($\delta^{15}\text{N}(\text{NO}_3^-)$), calculated atmospheric $\delta^{15}\text{N}$ of NO_x ($\delta^{15}\text{N}(\text{NO}_x)$), and $\delta^{15}\text{N}$
 764 shift between $\delta^{15}\text{N}(\text{NO}_3^-)$ and $\delta^{15}\text{N}(\text{NO}_2)$ ($\Delta^{15}(\text{NO}_3^- - \text{NO}_2)$).

765 4 Summary and implications

766 This study reports the first simultaneous measurements and analysis of $\Delta^{17}\text{O}$ and $\delta^{15}\text{N}$ in NO_2 and NO_3^- . The samplings were
 767 conducted at high temporal resolution (~ 3 h) in Chamonix, French Alps, over two distinct days in late February 2021. The
 768 isotopic signals of both NO_2 and NO_3^- show substantial diurnal variabilities which are investigated in the light of local
 769 meteorological parameters and atmospheric observations (NO , NO_2 , O_3 , and PM).

770

771 The observed variability of $\Delta^{17}\text{O}(\text{NO}_2)$ can be well explained using $\Delta^{17}\text{O}$ mass balance equations and corroborates the
772 analysis of previous observations carried out in Grenoble, French Alps, over a single day in spring (Albertin et al., 2021). On
773 average, the high levels of NO_2 at our site are primarily driven by oxidation of local NO emissions by O_3 . The observed
774 diurnal variability in $\Delta^{17}\text{O}(\text{NO}_2)$ appears to be consistent with the diurnal variability expected in the $\text{NO}_x/\text{O}_3/\text{RO}_2$ chemistry
775 with RO_2 levels of the order of pmol mol^{-1} which is in agreement with the range of direct winter RO_2 measurements reported
776 in the literature. RO_2 is thought to contribute significantly to the formation of NO_2 in the early morning under high- NO_x
777 conditions, which is in line with effective morning production of radical species reported in urban areas in winter. At night,
778 $\Delta^{17}\text{O}(\text{NO}_2)$ reflects the nocturnal oxidation of surface NO emissions by O_3 . These results provide additional evidence that
779 $\Delta^{17}\text{O}(\text{NO}_2)$ measurements represent valuable constraints in the study of the reactive NO_x chemistry, down to the sub-daily
780 temporal scales.

781

782 A clear linear relationship is found between $\delta^{15}\text{N}(\text{NO}_2)$ and the NO_2/NO_x ratio, indicating significant post-emission N
783 fractionation effects. Theoretical N isotopic fractionation factors between NO and NO_2 at equilibrium and fractionation
784 factors derived from the isotopic observations are found to be in good agreement, providing further support for the N
785 isotopic fractionation theoretical framework commonly applied to the Leighton cycle. Observed $\delta^{15}\text{N}(\text{NO}_2)$ corrected for N
786 fractionation effects allow to estimate the overall $\delta^{15}\text{N}$ signature of ambient NO_x at our site. Based on the existing $\delta^{15}\text{N}$ -
787 fingerprints of different NO_x emission sources, the main contribution at our site is very likely to be vehicle exhaust, which is
788 confirmed by local emission inventories.

789

790 We use $\Delta^{17}\text{O}$ mass balance equations of NO_3^- constrained by observed $\Delta^{17}\text{O}(\text{NO}_2)$ to assess whether NO_3^- could
791 originate locally from the oxidation of NO_2 at our site. During the first day of sampling, $\Delta^{17}\text{O}$ records of NO_2 and NO_3^-
792 support the local oxidation of NO_2 to NO_3^- by OH radicals during the day, and via the heterogeneous hydrolysis of N_2O_5
793 during the night. The second day of sampling was affected by a Saharan dust event, accompanied by notable changes in the
794 isotopic composition of NO_3^- . We propose that the formation of a surface inversion layer at night could have influenced the
795 vertical distribution of $\Delta^{17}\text{O}(\text{NO}_2)$ and resulted in a positive gradient of $\Delta^{17}\text{O}(\text{NO}_3^-)$ with altitude, independently of the local
796 NO_2 to NO_3^- conversion processes near the surface. In such scenario, the presence of Saharan dust could have promoted
797 heterogeneous NO_2 oxidation leading to higher $\Delta^{17}\text{O}$ in NO_3^- formed aloft. The latter would have then mixed with the NO_3^-
798 formed near the surface when the inversion breaks up during the day. Although still uncertain, the influence of the boundary
799 layer dynamics on the distribution of $\Delta^{17}\text{O}$ in NO_3^- should be investigated in the future, notably for urban areas in winter.

800

801 The combined analysis of the first concurrent observations of $\delta^{15}\text{N}$ in NO_2 and NO_3^- highlights persistent uncertainties
802 in the current estimates of the N fractionation factors associated with NO_2 and NO_3^- conversion processes. However,

803 $\delta^{15}\text{N}(\text{NO}_3^-)$ records need to be corrected for N fractionation effects if they are to be used to trace back the $\delta^{15}\text{N}$ fingerprint of
804 the primary NO_x emission sources. Detailed simulation chamber experiments could provide more kinetic data on the various
805 N fractionation processes in order to better exploit $\delta^{15}\text{N}(\text{NO}_3^-)$ records to identify and quantify of the sources of reactive
806 nitrogen.

807

808 The present thorough investigation of the $\Delta^{17}\text{O}$ and $\delta^{15}\text{N}$ in NO_2 and NO_3^- highlights (1) the potential to use sub-daily
809 $\Delta^{17}\text{O}$ and $\delta^{15}\text{N}$ records to trace the sources and formation chemistry of NO_3^- , (2) the importance of measuring the NO_2
810 isotopic composition to avoid misinterpretation of NO_3^- isotopic records, and (3) the persistent knowledge gaps that prevent
811 a complete assessment of the factors driving the variability in NO_3^- isotopic records. In most studies, the NO_3^- isotopic
812 composition is interpreted on the basis of estimates of the isotopic composition of its precursor gases, assuming that both the
813 chemistry of NO_2 (including its conversion to NO_3^-) and N isotopic fractionation effects are known. However, these
814 assumptions are subject to very significant uncertainties, mainly in urban atmospheres. Hence, given the recent development
815 of a method for measuring the multi-isotopic composition of NO_2 , the accuracy and validity of the current interpretation
816 framework of NO_3^- isotopic records should be tested in various environments. Such investigation can be performed by
817 collecting simultaneously NO_2 and NO_3^- , as done here. We recommend to use this combined isotopic in order to avoid
818 biased interpretations of NO_3^- isotopic records, particularly in urban areas during winter, and preferably at high temporal
819 resolution (<24 h). In addition, the vertical distribution of NO_2 and NO_3^- isotopic composition should be documented in
820 order to explore the possible role of the boundary layer dynamics in the variability of NO_2 and NO_3^- isotopic composition
821 observed at the surface.

822

823 5 Appendix A: Reaction chemical rate

Reactions	Rate constants /cm ³ mol ⁻¹ s ⁻¹	References
NO + O ₃ → NO ₂ + O ₂	$k_{\text{NO}+\text{O}_3} = 1.4 \times 10^{-12} \exp(-1310(\text{K})/T)$	Atkinson et al. (2004)
NO + RO ₂ → NO ₂ + RO	$k_{\text{NO}+\text{RO}_2} = 2.3 \times 10^{-12} \exp(360(\text{K})/T)$	Atkinson et al. (2006)
NO ₂ + O ₃ $\xrightarrow{\text{M}}$ NO ₃ + O ₂	$k_{\text{NO}_2+\text{O}_3} = 1.4 \times 10^{-13} \exp(-2470(\text{K})/T)$	Atkinson et al. (2004)
¹⁵ NO ₂ + ¹⁴ NO → ¹⁴ NO ₂ + ¹⁵ NO	$k_{\text{NO}+\text{NO}_2} = 8.14 \times 10^{-14}$	Sharma et al. (1970)

824 **Table A1.** Kinetic constants used in this study.825 6 Appendix B: Atmospheric lifetime of NO₂ and NO₃⁻

	$\tau_{\text{NO}_2}^{(1)}$	$\tau_{\text{NO}_3^-}^{(2)}$	$k_{\text{d}(\text{NO}_2)} \text{ (s}^{-1}\text{)}$	$k_{\text{d}(\text{NO}_3^-)} \text{ (s}^{-1}\text{)}$
Daytime (7:30–18:00)	5.1 min	27.8 h	0.5×10^{-5}	1.0×10^{-5}
Nighttime (18:00–07:30)	10.0 h	5.6 h	2.5×10^{-5}	5.0×10^{-5}

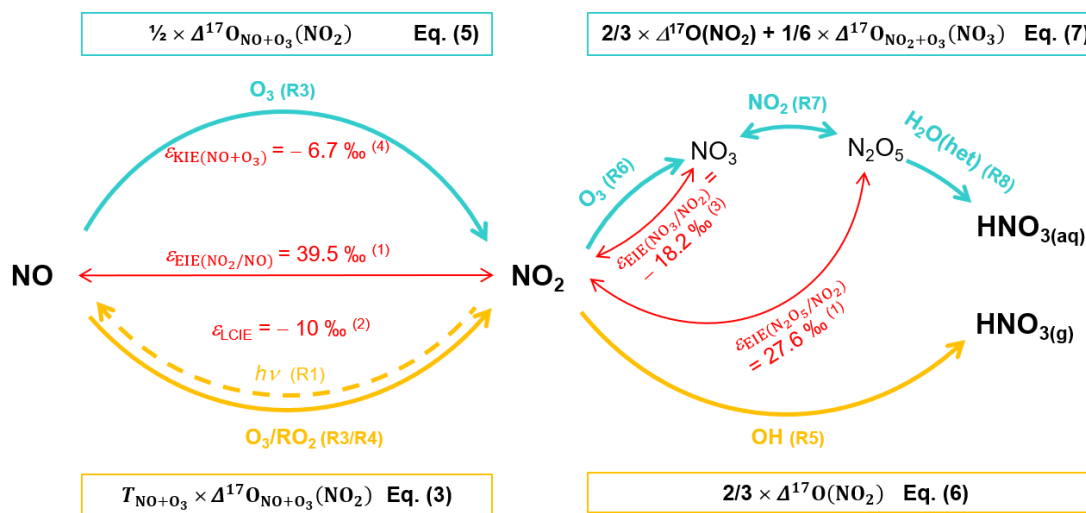
⁽¹⁾ Atmospheric lifetime relative to photolysis during the day (dry deposition and reaction NO₂ + OH are negligible) and to dry deposition and oxidation via O₃ during the night.

⁽²⁾ Atmospheric lifetime relative to dry deposition

The boundary layer is fixed at 500 m during the day and at 100 m during the night. Dry deposition velocity (V_d) is fixed at 0.25 cm s⁻¹ and 0.50 cm s⁻¹ for NO₂ and NO₃⁻, respectively (Holland et al., 1999; Zhang et al., 2009).

826 **Table B1.** Mean daytime (07:30–18:00 LT) and nighttime (18:00–07:30 LT) atmospheric lifetime of NO₂ (τ_{NO_2}) and NO₃⁻ ($\tau_{\text{NO}_3^-}$) and dry
827 deposition constant ($k_d = V_d \times \text{BLH}$ where V_d is the dry deposition velocity and BLH is the boundary layer height).

828 7 Appendix C: Schematic of the N reactive cycle and associated $\Delta^{17}\text{O}$ transfers and N enrichment factors



829

830 (1) Calculated at 298 K (Walters and Michalski, 2015)

831 (2) Experimental study at 298 K (Li et al., 2020)

832 (3) Calculated at 298 K (Walters et al., 2016)

833 (4) Calculated at 298 K (Fang et al., 2021)

834 **Figure C1.** Adapted from Elliott et al., (2019). Sketch of dominant daytime (thick yellow arrows) and nighttime (thick cyan arrows) NO_x
 835 to NO_3^- conversion processes and associated quantified N fractionation effects at 298 K (thin red arrows and text) and $\Delta^{17}\text{O}$ transfers
 836 (yellow and cyan boxes)

837 8 Appendix D: Equilibrium N fractionation factors

X/Y	A	B	C	D
NO_2/NO	3.847	-7.680	6.003	-0.118
$\text{N}_2\text{O}_5/\text{NO}_2$	1.004	-2.525	2.718	0.135

X + Y	A	B
$\text{NO} + \text{O}_3$	0.982	3.352

838

839 **Table D1.** Calculated regression coefficients for the N isotope exchange between NO_2/NO and $\text{N}_2\text{O}_5/\text{NO}_2$ over the temperature range of
 840 150 to 450 K (Walters and Michalski, 2015) and for the N kinetic fractionation for the reaction $\text{NO} + \text{O}_3$ over the temperature range of 220
 841 to 320 K (Fang et al., 2021).

842 **9 Data availability**

843 Data presented in this article are included in the Supplement.

844 **10 Author contributions.**

845 Grants obtained by KL and JS funded the project. AB, RB, QF, and IV performed the calibration of IBBCEAS and OFCEAS
846 instruments, data acquisition and post-processing. SA conducted the sampling and laboratory analysis. NC provided
847 technical support for isotopic mass spectrometry analysis. The study was designed as part of SA's PhD thesis supervised by
848 SB and JS. The paper was written by SA under the supervision of JS and SB and contributions from all co-authors.

849 **11 Competing interests.**

850 The authors declare that they have no conflict of interest.

851 **12 Acknowledgements.**

852 This work benefited from CNRS and IGE infrastructures and laboratory platforms. The authors acknowledge the support of
853 the CASPA program (Climate-relevant Aerosol Sources and Processes in the Arctic). The authors gratefully acknowledge
854 Catherine Coulaud for providing temperature data in Chamonix, Jean-Luc Jaffrezo for providing data of previous filter
855 measurements in Chamonix, and Anthony Lemoine, Matthieu Lafaysse and Louis Le Toumelin for providing S2M
856 reanalysis and meteorological data. The authors particularly thanks Patrick Ginot, Anthony Vella, Armelle Crouzet, and
857 Bruno Jourdain for instrumental and laboratory technical support. Finally, the authors thank Alexis Lamothe for assistance
858 during the sampling campaign and Pete Akers for his thorough proofreading of the manuscript and his constructive
859 comments.

860 **13 Financial support.**

861 This research has been supported by the Agence Nationale de la Recherche (ANR) via contract ANR-21-CE01-0017 CASPA
862 and INSU-CNRS (National Institute of Sciences of the Universe) via its national LEFE program (Les Enveloppes Fluides et
863 l'Environnement) and by a grant from Labex OSUG@2020 (Investissements d'avenir – ANR10 LABX56) and IDEX-UGA
864 ANR project ANR-15-IDEX-02.

865

866 **14 References**

- 867 Albertin, S., Savarino, J., Bekki, S., Barbero, A., and Caillon, N.: Measurement report: Nitrogen isotopes ($\delta^{15}\text{N}$) and first
868 quantification of oxygen isotope anomalies ($\Delta^{17}\text{O}$, $\delta^{18}\text{O}$) in atmospheric nitrogen dioxide, *Atmospheric Chemistry and*
869 *Physics*, 21, 10477–10497, <https://doi.org/10.5194/acp-21-10477-2021>, 2021.
- 870 Alexander, B., Hastings, M. G., Allman, D. J., Dachs, J., Thornton, J. A., and Kunasek, S. A.: Quantifying atmospheric
871 nitrate formation pathways based on a global model of the oxygen isotopic composition ($\Delta^{17}\text{O}$) of atmospheric nitrate,
872 *Atmospheric Chemistry and Physics*, 9, 5043–5056, <https://doi.org/10.5194/acp-9-5043-2009>, 2009.
- 873 Alexander, B., Sherwen, T., Holmes, C. D., Fisher, J. A., Chen, Q., Evans, M. J., and Kasibhatla, P.: Global inorganic nitrate
874 production mechanisms: comparison of a global model with nitrate isotope observations, *Atmospheric Chemistry and*
875 *Physics*, 20, 3859–3877, <https://doi.org/10.5194/acp-20-3859-2020>, 2020.
- 876 Aliche, B., Geyer, A., Hofzumahaus, A., Holland, F., Konrad, S., Pätz, H. W., Schäfer, J., Stutz, J., Volz-Thomas, A., and
877 Platt, U.: OH formation by HONO photolysis during the BERLIOZ experiment, *Journal of Geophysical Research:*
878 *Atmospheres*, 108, PHO 3-1-PHO 3-17, <https://doi.org/10.1029/2001JD000579>, 2003.
- 879 Allard, J.: Qualité de l'air dans la Vallée de l'Arve : météorologie locale et mesures des réductions des émissions liées au
880 chauffage au bois, PhD Thesis, Université Grenoble Alpes, 2018.
- 881 Ammann, M., Siegwolf, R., Pichlmayer, F., Suter, M., Saurer, M., and Brunold, C.: Estimating the uptake of traffic-derived
882 NO_2 from ^{15}N abundance in Norway spruce needles, *Oecologia*, 118, 124–131, <https://doi.org/10.1007/s004420050710>,
883 1999.
- 884 Angelisi, M. D. and Gaudichet, A.: Saharan dust deposition over Mont Blanc (French Alps) during the last 30 years, *Tellus*
885 *B*, 43, 61–75, <https://doi.org/10.1034/j.1600-0889.1991.00005.x>, 1991.
- 886 Appel, B. R., Wall, S. M., Tokiwa, Y., and Haik, M.: Simultaneous nitric acid, particulate nitrate and acidity measurements
887 in ambient air, *Atmospheric Environment*, 14, 549–554, [https://doi.org/10.1016/0004-6981\(80\)90084-0](https://doi.org/10.1016/0004-6981(80)90084-0), 1980.
- 888 Appel, B. R., Tokiwa, Y., and Haik, M.: Sampling of nitrates in ambient air, *Atmospheric Environment*, 15, 283–289,
889 [https://doi.org/10.1016/0004-6981\(81\)90029-9](https://doi.org/10.1016/0004-6981(81)90029-9), 1981.
- 890 Atkinson, R., Baulch, D. L., Cox, R. A., Crowley, J. N., Hampson, R. F., Hynes, R. G., Jenkin, M. E., Rossi, M. J., and Troe,
891 J.: Evaluated kinetic and photochemical data for atmospheric chemistry: Volume I - gas phase reactions of O_x , HO_x , NO_x and
892 SO_x species, *Atmospheric Chemistry and Physics*, 4, 1461–1738, <https://doi.org/10.5194/acp-4-1461-2004>, 2004.
- 893 Atkinson, R., Baulch, D. L., Cox, R. A., Crowley, J. N., Hampson, R. F., Hynes, R. G., Jenkin, M. E., Rossi, M. J., Troe, J.,
894 and IUPAC Subcommittee: Evaluated kinetic and photochemical data for atmospheric chemistry: Volume II - gas phase
895 reactions of organic species, *Atmospheric Chemistry and Physics*, 6, 3625–4055, <https://doi.org/10.5194/acp-6-3625-2006>,
896 2006.
- 897 Atmo-Auvergne-Rhône-Alpes: Bilan des connaissances sur la qualité de l'air dans la vallée de l'Arve, Atmo-Auvergne-
898 Rhône-Alpes, [https://www.atmo-auvergnerhonealpes.fr/publications/bilan-des-connaissances-sur-la-qualite-de-lair-dans-la-](https://www.atmo-auvergnerhonealpes.fr/publications/bilan-des-connaissances-sur-la-qualite-de-lair-dans-la-vallee-de-larve)
899 [vallee-de-larve](https://www.atmo-auvergnerhonealpes.fr/publications/bilan-des-connaissances-sur-la-qualite-de-lair-dans-la-vallee-de-larve), 2018.
- 900 Aumont, B., Chervier, F., and Laval, S.: Contribution of HONO sources to the $\text{NO}_x/\text{HO}_x/\text{O}_3$ chemistry in the polluted
901 boundary layer, *Atmospheric Environment*, 37, 487–498, [https://doi.org/10.1016/S1352-2310\(02\)00920-2](https://doi.org/10.1016/S1352-2310(02)00920-2), 2003.

- 902 Aymoz, G., Jaffrezo, J.-L., Jacob, V., Colomb, A., and George, C.: Evolution of organic and inorganic components of
903 aerosol during a Saharan dust episode observed in the French Alps, *Atmospheric Chemistry and Physics*, 4, 2499–2512,
904 <https://doi.org/10.5194/acp-4-2499-2004>, 2004.
- 905 Aymoz, G., Jaffrezo, J. L., Chapuis, D., Cozic, J., and Maenhaut, W.: Seasonal variation of PM₁₀ main constituents in two
906 valleys of the French Alps. I: EC/OC fractions, *Atmospheric Chemistry and Physics*, 7, 661–675,
907 <https://doi.org/10.5194/acp-7-661-2007>, 2007.
- 908 Barbero, A., Blouzon, C., Savarino, J., Caillon, N., Dommergue, A., and Grilli, R.: A compact incoherent broadband cavity-
909 enhanced absorption spectrometer for trace detection of nitrogen oxides, iodine oxide and glyoxal at levels below parts per
910 billion for field applications, *Atmospheric Measurement Techniques*, 13, 4317–4331, [https://doi.org/10.5194/amt-13-4317-](https://doi.org/10.5194/amt-13-4317-2020)
911 2020, 2020.
- 912 Barkan, E. and Luz, B.: High-precision measurements of ¹⁷O/¹⁶O and ¹⁸O/¹⁶O of O₂ and O₂/Ar ratio in air, *Rapid Commun.*
913 *Mass Spectrom.*, 17, 2809–2814, <https://doi.org/10.1002/rcm.1267>, 2003.
- 914 Bauer, S. E., Koch, D., Unger, N., Metzger, S. M., Shindell, D. T., and Streets, D. G.: Nitrate aerosols today and in 2030: a
915 global simulation including aerosols and tropospheric ozone, *Atmos. Chem. Phys.*, 7, 5043–5059,
916 <https://doi.org/10.5194/acp-7-5043-2007>, 2007.
- 917 Bekker, C., Walters, W. W., Murray, L. T., and Hastings, M. G.: Nitrate chemistry in the northeast US – Part 1: Nitrogen
918 isotope seasonality tracks nitrate formation chemistry, *Atmospheric Chemistry and Physics*, 23, 4185–4201,
919 <https://doi.org/10.5194/acp-23-4185-2023>, 2023.
- 920 Berhanu, T. A., Savarino, J., Bhattacharya, S. K., and Vicars, W. C.: ¹⁷O excess transfer during the NO₂ + O₃ → NO₃ + O₂
921 reaction, *The Journal of Chemical Physics*, 136, 044311, <https://doi.org/10.1063/1.3666852>, 2012.
- 922 Brown, S. S.: Variability in Nocturnal Nitrogen Oxide Processing and Its Role in Regional Air Quality, *Science*, 311, 67–70,
923 <https://doi.org/10.1126/science.1120120>, 2006.
- 924 Brown, S. S. and Stutz, J.: Nighttime radical observations and chemistry, *Chem Soc Rev*, 41, 6405–6447,
925 <https://doi.org/10.1039/c2cs35181a>, 2012.
- 926 Brown, S. S., Dubé, W. P., Peischl, J., Ryerson, T. B., Atlas, E., Warneke, C., de Gouw, J. A., te Lintel Hekkert, S., Brock,
927 C. A., Flocke, F., Trainer, M., Parrish, D. D., Feshenfeld, F. C., and Ravishankara, A. R.: Budgets for nocturnal VOC
928 oxidation by nitrate radicals aloft during the 2006 Texas Air Quality Study, *Journal of Geophysical Research: Atmospheres*,
929 116, <https://doi.org/10.1029/2011JD016544>, 2011.
- 930 Brulfert, G., Chemel, C., Chaxel, E., and Chollet, J. P.: Modelling photochemistry in alpine valleys, *Atmos. Chem. Phys.*,
931 <https://doi.org/10.5194/acp-5-2341-2005>, 2005.
- 932 Casciotti, K. L., Sigman, D. M., Hastings, M. G., Böhlke, J. K., and Hilkert, A.: Measurement of the oxygen isotopic
933 composition of nitrate in seawater and freshwater using the denitrifier method, *Analytical Chemistry*, 74, 4905–4912,
934 <https://doi.org/10.1021/ac020113w>, 2002.
- 935 Chan, Y.-C., Evans, M. J., He, P., Holmes, C. D., Jaeglé, L., Kasibhatla, P., Liu, X.-Y., Sherwen, T., Thornton, J. A., Wang,
936 X., Xie, Z., Zhai, S., and Alexander, B.: Heterogeneous Nitrate Production Mechanisms in Intense Haze Events in the North
937 China Plain, *Journal of Geophysical Research: Atmospheres*, 126, e2021JD034688, <https://doi.org/10.1029/2021JD034688>,
938 2021.

- 939 Chang, Y., Zhang, Y., Tian, C., Zhang, S., Ma, X., Cao, F., Liu, X., Zhang, W., Kuhn, T., and Lehmann, M. F.: Nitrogen
940 isotope fractionation during gas-to-particle conversion of NO_x to NO_3^- in the atmosphere – implications for isotope-based
941 NO_x source apportionment, *Atmospheric Chemistry and Physics*, 18, 11647–11661, [https://doi.org/10.5194/acp-18-11647-](https://doi.org/10.5194/acp-18-11647-2018)
942 2018, 2018.
- 943 Chazette, P., Couvert, P., Randriamiarisoa, H., Sanak, J., Bonsang, B., Moral, P., Berthier, S., Salanave, S., and Toussaint,
944 F.: Three-dimensional survey of pollution during winter in French Alps valleys, *Atmospheric Environment*, 39, 1035–1047,
945 <https://doi.org/10.1016/j.atmosenv.2004.10.014>, 2005.
- 946 Crutzen, P. J.: The Role of NO and NO_2 in the Chemistry of the Troposphere and Stratosphere, *Annu. Rev. Earth Planet.*
947 *Sci.*, 7, 443–472, <https://doi.org/10.1146/annurev.ea.07.050179.002303>, 1979.
- 948 Delmas, R. J.: Snow chemistry of high altitude glaciers in the French Alps, 46, 304,
949 <https://doi.org/10.3402/tellusb.v46i4.15806>, 1994.
- 950 Dentener, F. J. and Crutzen, P. J.: Reaction of N_2O_5 on tropospheric aerosols: Impact on the global distributions of NO_x ,
951 O_3 , and OH , *Journal of Geophysical Research: Atmospheres*, 98, 7149–7163, <https://doi.org/10.1029/92JD02979>, 1993.
- 952 Di Mauro, B., Garzonio, R., Rossini, M., Filippa, G., Pogliotti, P., Galvagno, M., Morra di Cella, U., Migliavacca, M.,
953 Baccolo, G., Clemenza, M., Delmonte, B., Maggi, V., Dumont, M., Tuzet, F., Lafaysse, M., Morin, S., Cremonese, E., and
954 Colombo, R.: Saharan dust events in the European Alps: role in snowmelt and geochemical characterization, *The*
955 *Cryosphere*, 13, 1147–1165, <https://doi.org/10.5194/tc-13-1147-2019>, 2019.
- 956 Dubey, M. K., Mohrshladt, R., Donahue, N. M., and Anderson, J. G.: Isotope Specific Kinetics of Hydroxyl Radical (OH)
957 with Water (H_2O): Testing Models of Reactivity and Atmospheric Fractionation, *J. Phys. Chem. A*, 101, 1494–1500,
958 <https://doi.org/10.1021/jp962332p>, 1997.
- 959 Edwards, P. M., Brown, S. S., Roberts, J. M., Ahmadov, R., Banta, R. M., deGouw, J. A., Dubé, W. P., Field, R. A., Flynn,
960 J. H., Gilman, J. B., Graus, M., Helmig, D., Koss, A., Langford, A. O., Lefer, B. L., Lerner, B. M., Li, R., Li, S.-M.,
961 McKeen, S. A., Murphy, S. M., Parrish, D. D., Senff, C. J., Soltis, J., Stutz, J., Sweeney, C., Thompson, C. R., Trainer, M.
962 K., Tsai, C., Veres, P. R., Washenfelder, R. A., Warneke, C., Wild, R. J., Young, C. J., Yuan, B., and Zamora, R.: High
963 winter ozone pollution from carbonyl photolysis in an oil and gas basin, *Nature*, 514, 351–354,
964 <https://doi.org/10.1038/nature13767>, 2014.
- 965 Elliott, E. M., Yu, Z., Cole, A. S., and Coughlin, J. G.: Isotopic advances in understanding reactive nitrogen deposition and
966 atmospheric processing, *Science of The Total Environment*, 662, 393–403, <https://doi.org/10.1016/j.scitotenv.2018.12.177>,
967 2019.
- 968 Emmerson, K. M., Carslaw, N., Carpenter, L. J., Heard, D. E., Lee, J. D., and Pilling, M. J.: Urban Atmospheric Chemistry
969 During the PUMA Campaign 1: Comparison of Modelled OH and HO_2 Concentrations with Measurements, *J Atmos Chem*,
970 52, 143–164, <https://doi.org/10.1007/s10874-005-1322-3>, 2005.
- 971 Fan, M.-Y., Zhang, Y.-L., Lin, Y.-C., Chang, Y.-H., Cao, F., Zhang, W.-Q., Hu, Y.-B., Bao, M.-Y., Liu, X.-Y., Zhai, X.-Y.,
972 Lin, X., Zhao, Z.-Y., and Song, W.-H.: Isotope-based source apportionment of nitrogen-containing aerosols: A case study in
973 an industrial city in China, *Atmospheric Environment*, 212, 96–105, <https://doi.org/10.1016/j.atmosenv.2019.05.020>, 2019.
- 974 Fan, M.-Y., Zhang, Y.-L., Lin, Y.-C., Hong, Y., Zhao, Z.-Y., Xie, F., Du, W., Cao, F., Sun, Y., and Fu, P.: Important Role of
975 NO_3 Radical to Nitrate Formation Aloft in Urban Beijing: Insights from Triple Oxygen Isotopes Measured at the Tower,
976 *Environ. Sci. Technol.*, 56, 6870–6879, <https://doi.org/10.1021/acs.est.1c02843>, 2022.

- 977 Fan, M.-Y., Zhang, W., Zhang, Y.-L., Li, J., Fang, H., Cao, F., Yan, M., Hong, Y., Guo, H., and Michalski, G.: Formation
978 Mechanisms and Source Apportionments of Nitrate Aerosols in a Megacity of Eastern China Based On Multiple Isotope
979 Observations, *Journal of Geophysical Research: Atmospheres*, 128, e2022JD038129, <https://doi.org/10.1029/2022JD038129>,
980 2023.
- 981 Fang, H., Walters, W. W., Mase, D., and Michalski, G.: i_N RACM: incorporating ^{15}N into the Regional Atmospheric
982 Chemistry Mechanism (RACM) for assessing the role photochemistry plays in controlling the isotopic composition of NO_x ,
983 NO_y , and atmospheric nitrate, *Geoscientific Model Development*, 14, 5001–5022, [https://doi.org/10.5194/gmd-14-5001-](https://doi.org/10.5194/gmd-14-5001-2021)
984 2021, 2021.
- 985 Felix, J. D. and Elliott, E. M.: Isotopic composition of passively collected nitrogen dioxide emissions: Vehicle, soil and
986 livestock source signatures, *Atmospheric Environment*, 92, 359–366, <https://doi.org/10.1016/j.atmosenv.2014.04.005>, 2014.
- 987 Felix, J. D., Elliott, E. M., and Shaw, S. L.: Nitrogen Isotopic Composition of Coal-Fired Power Plant NO_x : Influence of
988 Emission Controls and Implications for Global Emission Inventories, *Environ. Sci. Technol.*, 46, 3528–3535,
989 <https://doi.org/10.1021/es203355v>, 2012.
- 990 Fibiger, D. L. and Hastings, M. G.: First Measurements of the Nitrogen Isotopic Composition of NO_x from Biomass
991 Burning, *Environ. Sci. Technol.*, 50, 11569–11574, <https://doi.org/10.1021/acs.est.6b03510>, 2016.
- 992 Finlayson-Pitts, B. J. and Pitts, J. N.: *Chemistry of the Upper and Lower Atmosphere*, Elsevier,
993 <https://doi.org/10.1016/B978-012257060-5/50003-4>, 2000.
- 994 Frey, M. M., Savarino, J., Morin, S., Erbland, J., and Martins, J. M. F.: Photolysis imprint in the nitrate stable isotope signal
995 in snow and atmosphere of East Antarctica and implications for reactive nitrogen cycling, *Atmospheric Chemistry and*
996 *Physics*, 9, 8681–8696, <https://doi.org/10.5194/acp-9-8681-2009>, 2009.
- 997 Freyer, H. D.: Seasonal variation of $^{15}\text{N}/^{14}\text{N}$ ratios in atmospheric nitrate species, *Tellus B*, 43, 30–44,
998 <https://doi.org/10.1034/j.1600-0889.1991.00003.x>, 1991.
- 999 Freyer, H. D., Kley, D., Volz-Thomas, A., and Kobel, K.: On the interaction of isotopic exchange processes with
1000 photochemical reactions in atmospheric oxides of nitrogen, *Journal of Geophysical Research: Atmospheres*, 98, 14791–
1001 14796, <https://doi.org/10.1029/93JD00874>, 1993.
- 1002 Fu, X., Wang, T., Gao, J., Wang, P., Liu, Y., Wang, S., Zhao, B., and Xue, L.: Persistent Heavy Winter Nitrate Pollution
1003 Driven by Increased Photochemical Oxidants in Northern China, *Environ. Sci. Technol.*, 54, 3881–3889,
1004 <https://doi.org/10.1021/acs.est.9b07248>, 2020.
- 1005 Galeazzo, T., Bekki, S., Martin, E., Savarino, J., and Arnold, S. R.: Photochemical box modelling of volcanic SO_2 oxidation:
1006 isotopic constraints, *Atmospheric Chemistry and Physics*, 18, 17909–17931, <https://doi.org/10.5194/acp-18-17909-2018>,
1007 2018.
- 1008 Galloway, J. N., Townsend, A. R., Erisman, J. W., Bekunda, M., Cai, Z., Freney, J. R., Martinelli, L. A., Seitzinger, S. P.,
1009 and Sutton, M. A.: Transformation of the Nitrogen Cycle: Recent Trends, Questions, and Potential Solutions, *Science*, 320,
1010 889–892, <https://doi.org/10.1126/science.1136674>, 2008.
- 1011 Gaudel, A., Cooper, O. R., Ancellet, G., Barret, B., Boynard, A., Burrows, J. P., Clerbaux, C., Coheur, P.-F., Cuesta, J.,
1012 Cuevas, E., Doniki, S., Dufour, G., Ebojje, F., Foret, G., Garcia, O., Granados-Muñoz, M. J., Hannigan, J. W., Hase, F.,
1013 Hassler, B., Huang, G., Hurtmans, D., Jaffe, D., Jones, N., Kalabokas, P., Kerridge, B., Kulawik, S., Latter, B., Leblanc, T.,
1014 Le Flochmoën, E., Lin, W., Liu, J., Liu, X., Mahieu, E., McClure-Begley, A., Neu, J. L., Osman, M., Palm, M., Petetin, H.,

- 1015 Petropavlovskikh, I., Querel, R., Rahn, N., Rozanov, A., Schultz, M. G., Schwab, J., Siddans, R., Smale, D., Steinbacher,
1016 M., Tanimoto, H., Tarasick, D. W., Thouret, V., Thompson, A. M., Trickl, T., Weatherhead, E., Wespes, C., Worden, H. M.,
1017 Vigouroux, C., Xu, X., Zeng, G., and Ziemke, J.: Tropospheric Ozone Assessment Report: Present-day distribution and
1018 trends of tropospheric ozone relevant to climate and global atmospheric chemistry model evaluation, *Elementa: Science of
1019 the Anthropocene*, 6, <https://doi.org/10.1525/elementa.291>, 2018.
- 1020 Geng, L., Alexander, B., Cole-Dai, J., Steig, E. J., Savarino, J., Sofen, E. D., and Schauer, A. J.: Nitrogen isotopes in ice core
1021 nitrate linked to anthropogenic atmospheric acidity change, *Proc. Natl. Acad. Sci. U.S.A.*, 111, 5808–5812,
1022 <https://doi.org/10.1073/pnas.1319441111>, 2014.
- 1023 Goudie, A. S. and Middleton, N. J.: Saharan dust storms: nature and consequences, *Earth-Science Reviews*, 56, 179–204,
1024 [https://doi.org/10.1016/S0012-8252\(01\)00067-8](https://doi.org/10.1016/S0012-8252(01)00067-8), 2001.
- 1025 Grannas, A. M., Jones, A. E., Dibb, J., Ammann, M., Anastasio, C., Beine, H. J., Bergin, M., Bottenheim, J., Boxe, C. S.,
1026 Carver, G., Chen, G., Crawford, J. H., Dominé, F., Frey, M. M., Guzmán, M. I., Heard, D. E., Helmig, D., Hoffmann, M. R.,
1027 Honrath, R. E., Huey, L. G., Hutterli, M., Jacobi, H. W., Klán, P., Lefer, B., McConnell, J., Plane, J., Sander, R., Savarino,
1028 J., Shepson, P. B., Simpson, W. R., Sodeau, J. R., von Glasow, R., Weller, R., Wolff, E. W., and Zhu, T.: An overview of
1029 snow photochemistry: evidence, mechanisms and impacts, *Atmospheric Chemistry and Physics*, 7, 4329–4373,
1030 <https://doi.org/10.5194/acp-7-4329-2007>, 2007.
- 1031 Greiling, M., Schauer, G., Baumann-Stanzer, K., Skomorowski, P., Schöner, W., and Kasper-Giebl, A.: Contribution of
1032 Saharan Dust to Ion Deposition Loads of High Alpine Snow Packs in Austria (1987–2017), *Frontiers in Earth Science*, 6,
1033 2018.
- 1034 Gu, P., Dallmann, T. R., Li, H. Z., Tan, Y., and Presto, A. A.: Quantifying Urban Spatial Variations of Anthropogenic VOC
1035 Concentrations and Source Contributions with a Mobile Sampling Platform, *Int J Environ Res Public Health*, 16,
1036 <https://doi.org/10.3390/ijerph16091632>, 2019.
- 1037 He, P., Xie, Z., Chi, X., Yu, X., Fan, S., Kang, H., Liu, C., and Zhan, H.: Atmospheric $\Delta^{17}\text{O}(\text{NO}_3^-)$ reveals nocturnal
1038 chemistry dominates nitrate production in Beijing haze, *Atmospheric Chemistry and Physics*, 18, 14465–14476,
1039 <https://doi.org/10.5194/acp-18-14465-2018>, 2018.
- 1040 He, P., Xie, Z., Yu, X., Wang, L., Kang, H., and Yue, F.: The observation of isotopic compositions of atmospheric nitrate in
1041 Shanghai China and its implication for reactive nitrogen chemistry, *Science of The Total Environment*, 714, 136727,
1042 <https://doi.org/10.1016/j.scitotenv.2020.136727>, 2020.
- 1043 Heaton, T. H. E.: $^{15}\text{N}/^{14}\text{N}$ ratios of NO_x from vehicle engines and coal-fired power stations, *Tellus B*, 42, 304–307,
1044 <https://doi.org/10.1034/j.1600-0889.1990.00007.x-i1>, 1990.
- 1045 Hoesly, R. M., Smith, S. J., Feng, L., Klimont, Z., Janssens-Maenhout, G., Pitkanen, T., Seibert, J. J., Vu, L., Andres, R. J.,
1046 Bolt, R. M., Bond, T. C., Dawidowski, L., Kholod, N., Kurokawa, J., Li, M., Liu, L., Lu, Z., Moura, M. C. P., O'Rourke, P.
1047 R., and Zhang, Q.: Historical (1750–2014) anthropogenic emissions of reactive gases and aerosols from the Community
1048 Emissions Data System (CEDS), *Geoscientific Model Development*, 11, 369–408, [https://doi.org/10.5194/gmd-11-369-
1049 2018](https://doi.org/10.5194/gmd-11-369-2018), 2018.
- 1050 Holland, E. A., Dentener, F. J., Braswell, B. H., and Sulzman, J. M.: Contemporary and pre-industrial global reactive
1051 nitrogen budgets, *Biogeochemistry*, 46, 7–43, <https://doi.org/10.1023/A:1006148011944>, 1999.
- 1052 Huang, R.-J., Zhang, Y., Bozzetti, C., Ho, K.-F., Cao, J.-J., Han, Y., Daellenbach, K. R., Slowik, J. G., Platt, S. M.,
1053 Canonaco, F., Zotter, P., Wolf, R., Pieber, S. M., Bruns, E. A., Crippa, M., Ciarelli, G., Piazzalunga, A., Schwikowski, M.,

- 1054 Abbaszade, G., Schnelle-Kreis, J., Zimmermann, R., An, Z., Szidat, S., Baltensperger, U., Haddad, I. E., and Prévôt, A. S.
1055 H.: High secondary aerosol contribution to particulate pollution during haze events in China, *Nature*, 514, 218–222,
1056 <https://doi.org/10.1038/nature13774>, 2014.
- 1057 Kaiser, J., Hastings, M. G., Houlton, B. Z., Röckmann, T., and Sigman, D. M.: Triple oxygen isotope analysis of nitrate
1058 using the denitrifier method and thermal decomposition of N₂O, *Anal. Chem.*, 79, 599–607,
1059 <https://doi.org/10.1021/ac061022s>, 2007.
- 1060 Kanaya, Y., Cao, R., Akimoto, H., Fukuda, M., Komazaki, Y., Yokouchi, Y., Koike, M., Tanimoto, H., Takegawa, N., and
1061 Kondo, Y.: Urban photochemistry in central Tokyo: 1. Observed and modeled OH and HO₂ radical concentrations during the
1062 winter and summer of 2004, *Journal of Geophysical Research: Atmospheres*, 112, <https://doi.org/10.1029/2007JD008670>,
1063 2007.
- 1064 Karydis, V. A., Tsimpidi, A. P., Pozzer, A., Astitha, M., and Lelieveld, J.: Effects of mineral dust on global atmospheric
1065 nitrate concentrations, *Atmospheric Chemistry and Physics*, 16, 1491–1509, <https://doi.org/10.5194/acp-16-1491-2016>,
1066 2016.
- 1067 Kim, H., Walters, W. W., Bekker, C., Murray, L. T., and Hastings, M. G.: Nitrate chemistry in the northeast US – Part 2:
1068 Oxygen isotopes reveal differences in particulate and gas-phase formation, *Atmospheric Chemistry and Physics*, 23, 4203–
1069 4219, <https://doi.org/10.5194/acp-23-4203-2023>, 2023.
- 1070 Kirchstetter, T. W., Harley, R. A., and Littlejohn, D.: Measurement of Nitrous Acid in Motor Vehicle Exhaust, *Environ. Sci.*
1071 *Technol.*, 30, 2843–2849, <https://doi.org/10.1021/es960135y>, 1996.
- 1072 Kurtenbach, R., Becker, K. H., Gomes, J. A. G., Kleffmann, J., Lörzer, J. C., Spittler, M., Wiesen, P., Ackermann, R., Geyer,
1073 A., and Platt, U.: Investigations of emissions and heterogeneous formation of HONO in a road traffic tunnel, *Atmospheric*
1074 *Environment*, 35, 3385–3394, [https://doi.org/10.1016/S1352-2310\(01\)00138-8](https://doi.org/10.1016/S1352-2310(01)00138-8), 2001.
- 1075 Llargeron, Y. and Staquet, C.: Persistent inversion dynamics and wintertime PM₁₀ air pollution in Alpine valleys,
1076 *Atmospheric Environment*, 135, 92–108, <https://doi.org/10.1016/j.atmosenv.2016.03.045>, 2016.
- 1077 Leighton, P. A.: *Photochemistry of Air Pollution.*, 66, 1961.
- 1078 Li, J., Zhang, X., Orlando, J., Tyndall, G., and Michalski, G.: Quantifying the nitrogen isotope effects during photochemical
1079 equilibrium between NO and NO₂: implications for $\delta^{15}\text{N}$ in tropospheric reactive nitrogen, *Atmospheric Chemistry and*
1080 *Physics*, 20, 9805–9819, <https://doi.org/10.5194/acp-20-9805-2020>, 2020.
- 1081 Li, J., Davy, P., Harvey, M., Katzman, T., Mitchell, T., and Michalski, G.: Nitrogen isotopes in nitrate aerosols collected in
1082 the remote marine boundary layer: Implications for nitrogen isotopic fractionations among atmospheric reactive nitrogen
1083 species, *Atmospheric Environment*, 245, 118028, <https://doi.org/10.1016/j.atmosenv.2020.118028>, 2021a.
- 1084 Li, K., Jacob, D. J., Liao, H., Qiu, Y., Shen, L., Zhai, S., Bates, K. H., Sulprizio, M. P., Song, S., Lu, X., Zhang, Q., Zheng,
1085 B., Zhang, Y., Zhang, J., Lee, H. C., and Kuk, S. K.: Ozone pollution in the North China Plain spreading into the late-winter
1086 haze season, *Proceedings of the National Academy of Sciences*, 118, e2015797118,
1087 <https://doi.org/10.1073/pnas.2015797118>, 2021b.
- 1088 Li, W., Ni, B. L., Jin, D. Q., and Zhang, Q. G.: Measurement of the absolute abundance of Oxygen-17 in SMOW, *Kexue*
1089 *Tongboa, Chinese Science Bulletin*, 33 (19), 1610–1613, <https://doi.org/10.1360/sb1988-33-19-1610>, 1988.

- 1090 Li, Y., Shi, G., Chen, Z., Lan, M., Ding, M., Li, Z., and Hastings, M. G.: Significant Latitudinal Gradient of Nitrate
1091 Production in the Marine Atmospheric Boundary Layer of the Northern Hemisphere, *Geophysical Research Letters*, 49,
1092 e2022GL100503, <https://doi.org/10.1029/2022GL100503>, 2022a.
- 1093 Li, Z., Walters, W. W., Hastings, M. G., Song, L., Huang, S., Zhu, F., Liu, D., Shi, G., Li, Y., and Fang, Y.: Atmospheric
1094 nitrate formation pathways in urban and rural atmosphere of Northeast China: Implications for complicated anthropogenic
1095 effects, *Environmental Pollution*, 296, 118752, <https://doi.org/10.1016/j.envpol.2021.118752>, 2022b.
- 1096 Lim, S., Lee, M., Savarino, J., and Laj, P.: Oxidation pathways and emission sources of atmospheric particulate nitrate in
1097 Seoul: based on $\delta^{15}\text{N}$ and $\Delta^{17}\text{O}$ measurements, *Atmospheric Chemistry and Physics*, 22, 5099–5115,
1098 <https://doi.org/10.5194/acp-22-5099-2022>, 2022.
- 1099 Liu, J., Liu, Z., Ma, Z., Yang, S., Yao, D., Zhao, S., Hu, B., Tang, G., Sun, J., Cheng, M., Xu, Z., and Wang, Y.: Detailed
1100 budget analysis of HONO in Beijing, China: Implication on atmosphere oxidation capacity in polluted megacity,
1101 *Atmospheric Environment*, 244, 117957, <https://doi.org/10.1016/j.atmosenv.2020.117957>, 2021.
- 1102 Liu, Z., Hu, K., Zhang, K., Zhu, S., Wang, M., and Li, L.: VOCs sources and roles in O₃ formation in the central Yangtze
1103 River Delta region of China, *Atmospheric Environment*, 302, 119755, <https://doi.org/10.1016/j.atmosenv.2023.119755>,
1104 2023.
- 1105 Luo, L., Wu, S., Zhang, R., Wu, Y., Li, J., and Kao, S.: What controls aerosol $\delta^{15}\text{N}$ -NO₃-? NO_x emission sources vs.
1106 nitrogen isotope fractionation, *Science of The Total Environment*, 871, 162185,
1107 <https://doi.org/10.1016/j.scitotenv.2023.162185>, 2023.
- 1108 Mariotti, A.: Natural ¹⁵N abundance measurements and atmospheric nitrogen standard calibration, *Nature*, 311, 251–252,
1109 <https://doi.org/10.1038/311251a0>, 1984.
- 1110 Masson-Delmotte, V., Zhai, A., Pirani, A., Connors, S. L., Péan, C., Berger, S., Caud, N., Chen, Y., Goldfarb, L., Gomis, M.
1111 I., Huang, M., Leitzell, K., Lonnoy, E., Matthews, J. B. R., Maycock, T. K., Waterfield, T., Yelekçi, O., Yu, R., and Zhou,
1112 B.: In *Climate Change 2021: The Physical Science Basis. Contribution of Working Group I to the Sixth Assessment Report*
1113 of the Intergovernmental Panel on Climate Change, Cambridge University Press, Cambridge, United Kingdom and New
1114 York, NY, USA, 147–286, <https://doi.org/10.1017/9781009157896.003>, 2021.
- 1115 Mayer, H.: Air pollution in cities, *Atmospheric Environment*, 33, 4029–4037, [https://doi.org/10.1016/S1352-2310\(99\)00144-](https://doi.org/10.1016/S1352-2310(99)00144-2)
1116 2, 1999.
- 1117 McIlvin, M. R. and Altabet, M. A.: Chemical Conversion of Nitrate and Nitrite to Nitrous Oxide for Nitrogen and Oxygen
1118 Isotopic Analysis in Freshwater and Seawater, *Analytical Chemistry*, 77, 5589–5595, <https://doi.org/10.1021/ac050528s>,
1119 2005.
- 1120 Michalski, G., Scott, Z., Kabling, M., and Thiemens, M. H.: First measurements and modeling of $\Delta^{17}\text{O}$ in atmospheric
1121 nitrate., *Geophysical Research Letters*, 30, 1870, <https://doi.org/10.1029/2003GL017015>, 2003.
- 1122 Michalski, G., Bhattacharya, S. K., and Girsch, G.: NO_x cycle and the tropospheric ozone isotope anomaly: an experimental
1123 investigation, *Atmospheric Chemistry and Physics*, 14, 4935–4953, <https://doi.org/10.5194/acp-14-4935-2014>, 2014.
- 1124 Michoud, V., Doussin, J.-F., Colomb, A., Afif, C., Borbon, A., Camredon, M., Aumont, B., Legrand, M., and Beekmann,
1125 M.: Strong HONO formation in a suburban site during snowy days, *Atmospheric Environment*, 116, 155–158,
1126 <https://doi.org/10.1016/j.atmosenv.2015.06.040>, 2015.

- 1127 Miller, C. E. and Yung, Y. L.: Photo-induced isotopic fractionation, *Journal of Geophysical Research: Atmospheres*, 105,
1128 29039–29051, <https://doi.org/10.1029/2000JD900388>, 2000.
- 1129 Miller, D. J., Wojtal, P. K., Clark, S. C., and Hastings, M. G.: Vehicle NO_x emission plume isotopic signatures: Spatial
1130 variability across the eastern United States, *Journal of Geophysical Research: Atmospheres*, 122, 4698–4717,
1131 <https://doi.org/10.1002/2016JD025877>, 2017.
- 1132 Miller, D. J., Chai, J., Guo, F., Dell, C. J., Karsten, H., and Hastings, M. G.: Isotopic Composition of In Situ Soil NO_x
1133 Emissions in Manure-Fertilized Cropland, *Geophysical Research Letters*, 45, 12,058–12,066,
1134 <https://doi.org/10.1029/2018GL079619>, 2018.
- 1135 Morin, S., Savarino, J., Bekki, S., Cavender, A., Shepson, P. B., and Bottenheim, J. W.: Major influence of BrO on the NO₃
1136 and nitrate budgets in the Arctic spring, inferred from $\Delta^{17}\text{O}(\text{NO}_3^-)$ measurements during ozone depletion events, *Environ.*
1137 *Chem.*, 4, 238, <https://doi.org/10.1071/EN07003>, 2007a.
- 1138 Morin, S., Savarino, J., Bekki, S., Gong, S., and Bottenheim, J. W.: Signature of Arctic surface ozone depletion events in the
1139 isotope anomaly ($\Delta^{17}\text{O}$) of atmospheric nitrate, *Atmos. Chem. Phys.*, 7, 1451–1469, [https://doi.org/10.5194/acp-7-1451-](https://doi.org/10.5194/acp-7-1451-2007)
1140 2007, 2007b.
- 1141 Morin, S., Savarino, J., Frey, M. M., Domine, F., Jacobi, H.-W., Kaleschke, L., and Martins, J. M. F.: Comprehensive
1142 isotopic composition of atmospheric nitrate in the Atlantic Ocean boundary layer from 65°S to 79°N, *Journal of Geophysical*
1143 *Research: Atmospheres*, 114, <https://doi.org/10.1029/2008JD010696>, 2009.
- 1144 Morin, S., Sander, R., and Savarino, J.: Simulation of the diurnal variations of the oxygen isotope anomaly ($\Delta^{17}\text{O}$) of reactive
1145 atmospheric species, *Atmospheric Chemistry and Physics*, 11, 3653–3671, <https://doi.org/10.5194/acp-11-3653-2011>, 2011.
- 1146 Newsome, B. and Evans, M.: Impact of uncertainties in inorganic chemical rate constants on tropospheric composition and
1147 ozone radiative forcing, *Atmos. Chem. Phys.*, 17, 14333–14352, <https://doi.org/10.5194/acp-17-14333-2017>, 2017.
- 1148 Olofson, K. F. G., Andersson, P. U., Hallquist, M., Ljungström, E., Tang, L., Chen, D., and Pettersson, J. B. C.: Urban
1149 aerosol evolution and particle formation during wintertime temperature inversions, *Atmospheric Environment*, 43, 340–346,
1150 <https://doi.org/10.1016/j.atmosenv.2008.09.080>, 2009.
- 1151 ORCAE: Rapport des profils climat air énergie de la communauté de communes de la Vallée de Chamonix-Mont-Blanc,
1152 <https://www.orcae-auvergne-rhone-alpes.fr/>, 2022.
- 1153 Park, R. J., Jacob, D. J., Field, B. D., Yantosca, R. M., and Chin, M.: Natural and transboundary pollution influences on
1154 sulfate-nitrate-ammonium aerosols in the United States: Implications for policy, *Journal of Geophysical Research:*
1155 *Atmospheres*, 109, <https://doi.org/10.1029/2003JD004473>, 2004.
- 1156 Patris, N., Cliff, S., Quinn, P., Kasem, M., and Thiemens, M.: Isotopic analysis of aerosol sulfate and nitrate during ITCT-
1157 2k2: Determination of different formation pathways as a function of particle size, *Journal of Geophysical Research*, 112,
1158 <https://doi.org/10.1029/2005JD006214>, 2007.
- 1159 Penkett, S. A., Burgess, R. A., Coe, H., Coll, I., Hov, Ø., Lindskog, A., Schmidbauer, N., Solberg, S., Roemer, M., Thijsse,
1160 T., Beck, J., and Reeves, C. E.: Evidence for large average concentrations of the nitrate radical (NO₃) in Western Europe
1161 from the HANSA hydrocarbon database, *Atmospheric Environment*, 41, 3465–3478,
1162 <https://doi.org/10.1016/j.atmosenv.2006.11.055>, 2007.

- 1163 Prabhakar, G., Parworth, C. L., Zhang, X., Kim, H., Young, D. E., Beyersdorf, A. J., Ziemba, L. D., Nowak, J. B., Bertram,
1164 T. H., Faloon, I. C., Zhang, Q., and Cappa, C. D.: Observational assessment of the role of nocturnal residual-layer
1165 chemistry in determining daytime surface particulate nitrate concentrations, *Atmospheric Chemistry and Physics*, 17, 14747–
1166 14770, <https://doi.org/10.5194/acp-17-14747-2017>, 2017.
- 1167 Prospero, J. M. and Savoie, D. L.: Effect of continental sources on nitrate concentrations over the Pacific Ocean, *Nature*,
1168 339, 687–689, <https://doi.org/10.1038/339687a0>, 1989.
- 1169 Pugh, T. A. M., Cain, M., Methven, J., Wild, O., Arnold, S. R., Real, E., Law, K. S., Emmerson, K. M., Owen, S. M., Pyle,
1170 J. A., Hewitt, C. N., and MacKenzie, A. R.: A Lagrangian model of air-mass photochemistry and mixing using a trajectory
1171 ensemble: the Cambridge Tropospheric Trajectory model of Chemistry And Transport (CiTTyCAT) version 4.2, *Geosci.*
1172 *Model Dev.*, 5, 193–221, <https://doi.org/10.5194/gmd-5-193-2012>, 2012.
- 1173 Quimbayo-Duarte, J., Chemel, C., Staquet, C., Troude, F., and Arduini, G.: Drivers of severe air pollution events in a deep
1174 valley during wintertime: A case study from the Arve river valley, France, *Atmospheric Environment*, 247, 118030,
1175 <https://doi.org/10.1016/j.atmosenv.2020.118030>, 2021.
- 1176 Ren, J., Guo, F., and Xie, S.: Diagnosing ozone–NO_x–VOC sensitivity and revealing causes of ozone increases in China
1177 based on 2013–2021 satellite retrievals, *Atmos. Chem. Phys.*, 22, 15035–15047, <https://doi.org/10.5194/acp-22-15035-2022>,
1178 2022.
- 1179 Ren, X., Brune, W. H., Mao, J., Mitchell, M. J., Leshner, R. L., Simpas, J. B., Metcalf, A. R., Schwab, J. J., Cai, C., Li, Y.,
1180 Demerjian, K. L., Felton, H. D., Boynton, G., Adams, A., Perry, J., He, Y., Zhou, X., and Hou, J.: Behavior of OH and HO₂
1181 in the winter atmosphere in New York City, *Atmospheric Environment*, 40, 252–263,
1182 <https://doi.org/10.1016/j.atmosenv.2005.11.073>, 2006.
- 1183 Richard, L., Romanini, D., and Ventrillard, I.: Nitric Oxide Analysis Down to ppt Levels by Optical-Feedback Cavity-
1184 Enhanced Absorption Spectroscopy, *Sensors*, 18, 1997, <https://doi.org/10.3390/s18071997>, 2018.
- 1185 Savard, M. M., Cole, A. S., Vet, R., and Smirnoff, A.: The $\Delta^{17}\text{O}$ and $\delta^{18}\text{O}$ values of atmospheric nitrates simultaneously
1186 collected downwind of anthropogenic sources – implications for polluted air masses, *Atmospheric Chemistry and Physics*,
1187 18, 10373–10389, <https://doi.org/10.5194/acp-18-10373-2018>, 2018.
- 1188 Savarino, J., Kaiser, J., Morin, S., Sigman, D. M., and Thiemens, M. H.: Nitrogen and oxygen isotopic constraints on the
1189 origin of atmospheric nitrate in coastal Antarctica, *Atmos. Chem. Phys.*, 21, 2007.
- 1190 Savarino, J., Bhattacharya, S. K., Morin, S., Baroni, M., and Doussin, J.-F.: The NO+O₃ reaction: A triple oxygen isotope
1191 perspective on the reaction dynamics and atmospheric implications for the transfer of the ozone isotope anomaly, *J. Chem.*
1192 *Phys.*, 128, 194303, <https://doi.org/10.1063/1.2917581>, 2008.
- 1193 Savarino, J., Morin, S., Erbland, J., Grannec, F., Patey, M. D., Vicars, W., Alexander, B., and Achterberg, E. P.: Isotopic
1194 composition of atmospheric nitrate in a tropical marine boundary layer, *PNAS*, 110, 17668–17673,
1195 <https://doi.org/10.1073/pnas.1216639110>, 2013.
- 1196 Savarino, J., Vicars, W. C., Legrand, M., Preunkert, S., Jourdain, B., Frey, M. M., Kukui, A., Caillon, N., and Roca, J. G.:
1197 Oxygen isotope mass balance of atmospheric nitrate at Dome C, East Antarctica, during the OPAL campaign, *Atmos.*
1198 *Chem. Phys.*, 16, 2016.
- 1199 Schaap, M., Müller, K., and ten Brink, H. M.: Constructing the European aerosol nitrate concentration field from quality
1200 analysed data, *Atmospheric Environment*, 36, 1323–1335, [https://doi.org/10.1016/S1352-2310\(01\)00556-8](https://doi.org/10.1016/S1352-2310(01)00556-8), 2002.

- 1201 Schwikowski, M., Seibert, P., Baltensperger, U., and Gaggeler, H. W.: A study of an outstanding Saharan dust event at the
1202 high-alpine site Jungfraujoch, Switzerland, *Atmospheric Environment*, 29, 1829–1842, [https://doi.org/10.1016/1352-](https://doi.org/10.1016/1352-1203)
1203 2310(95)00060-C, 1995.
- 1204 Shah, V., Jaeglé, L., Thornton, J. A., Lopez-Hilfiker, F. D., Lee, B. H., Schroder, J. C., Campuzano-Jost, P., Jimenez, J. L.,
1205 Guo, H., Sullivan, A. P., Weber, R. J., Green, J. R., Fiddler, M. N., Bililign, S., Campos, T. L., Stell, M., Weinheimer, A. J.,
1206 Montzka, D. D., and Brown, S. S.: Chemical feedbacks weaken the wintertime response of particulate sulfate and nitrate to
1207 emissions reductions over the eastern United States, *Proc Natl Acad Sci USA*, 115, 8110–8115,
1208 <https://doi.org/10.1073/pnas.1803295115>, 2018.
- 1209 Sharma, H. D., Jarvis, R. E., and Wong, K. Y.: Isotopic exchange reactions in nitrogen oxides, *J. Phys. Chem.*, 74, 923–933,
1210 <https://doi.org/10.1021/j100699a044>, 1970.
- 1211 Shi, X., Nenes, A., Xiao, Z., Song, S., Yu, H., Shi, G., Zhao, Q., Chen, K., Feng, Y., and Russell, A. G.: High-Resolution
1212 Data Sets Unravel the Effects of Sources and Meteorological Conditions on Nitrate and Its Gas-Particle Partitioning,
1213 *Environ. Sci. Technol.*, 53, 3048–3057, <https://doi.org/10.1021/acs.est.8b06524>, 2019.
- 1214 Sigman, D. M., Casciotti, K. L., Andreani, M., Barford, C., Galanter, M., and Böhlke, J. K.: A Bacterial Method for the
1215 Nitrogen Isotopic Analysis of Nitrate in Seawater and Freshwater, *Analytical Chemistry*, 73, 4145–4153,
1216 <https://doi.org/10.1021/ac010088e>, 2001.
- 1217 Simpson, W. R., Brown, S. S., Saiz-Lopez, A., Thornton, J. A., and von Glasow, R.: Tropospheric Halogen Chemistry:
1218 Sources, Cycling, and Impacts, *Chem. Rev.*, 115, 4035–4062, <https://doi.org/10.1021/cr5006638>, 2015.
- 1219 Sodemann, H., Palmer, A. S., Schwierz, C., Schwikowski, M., and Wernli, H.: The transport history of two Saharan dust
1220 events archived in an Alpine ice core, *Atmospheric Chemistry and Physics*, 6, 667–688, [https://doi.org/10.5194/acp-6-667-](https://doi.org/10.5194/acp-6-667-2006)
1221 2006, 2006.
- 1222 Song, W., Liu, X.-Y., Houlton, B. Z., and Liu, C.-Q.: Isotopic constraints confirm the significant role of microbial nitrogen
1223 oxides emissions from the land and ocean environment, *National Science Review*, 9, nwac106,
1224 <https://doi.org/10.1093/nsr/nwac106>, 2022.
- 1225 Stone, D., Whalley, L. K., and Heard, D. E.: Tropospheric OH and HO₂ radicals: field measurements and model
1226 comparisons, *Chem. Soc. Rev.*, 41, 6348–6404, <https://doi.org/10.1039/C2CS35140D>, 2012.
- 1227 Tan, Z., Rohrer, F., Lu, K., Ma, X., Bohn, B., Broch, S., Dong, H., Fuchs, H., Gkatzelis, G. I., Hofzumahaus, A., Holland, F.,
1228 Li, X., Liu, Y., Liu, Y., Novelli, A., Shao, M., Wang, H., Wu, Y., Zeng, L., Hu, M., Kiendler-Scharr, A., Wahner, A., and
1229 Zhang, Y.: Wintertime photochemistry in Beijing: observations of RO_x radical concentrations in the North China Plain
1230 during the BEST-ONE campaign, *Atmos. Chem. Phys.*, 18, 12391–12411, <https://doi.org/10.5194/acp-18-12391-2018>, 2018.
- 1231 Thiemens, M. H.: History and Applications of Mass-independent Isotope Effects, *Annual Review of Earth and Planetary*
1232 *Sciences*, 34, 217–262, <https://doi.org/10.1146/annurev.earth.34.031405.125026>, 2006.
- 1233 Thornton, J. A., Kercher, J. P., Riedel, T. P., Wagner, N. L., Cozic, J., Holloway, J. S., Dubé, W. P., Wolfe, G. M., Quinn, P.
1234 K., Middlebrook, A. M., Alexander, B., and Brown, S. S.: A large atomic chlorine source inferred from mid-continental
1235 reactive nitrogen chemistry, *Nature*, 464, 271–274, <https://doi.org/10.1038/nature08905>, 2010.
- 1236 Tørseth, K., Aas, W., Breivik, K., Fjæraa, A. M., Fiebig, M., Hjellbrekke, A. G., Lund Myhre, C., Solberg, S., and Yttri, K.
1237 E.: Introduction to the European Monitoring and Evaluation Programme (EMEP) and observed atmospheric composition

- 1238 change during 1972-2009, *Atmospheric Chemistry and Physics*, 12, 5447–5481, <https://doi.org/10.5194/acp-12-5447-2012>,
1239 2012.
- 1240 Tsimpidi, A. P., Karydis, V. A., and Pandis, S. N.: Response of Fine Particulate Matter to Emission Changes of Oxides of
1241 Nitrogen and Anthropogenic Volatile Organic Compounds in the Eastern United States, *Journal of the Air & Waste*
1242 *Management Association*, 58, 1463–1473, <https://doi.org/10.3155/1047-3289.58.11.1463>, 2008.
- 1243 Usher, C. R., Michel, A. E., and Grassian, V. H.: Reactions on Mineral Dust, *Chem. Rev.*, 103, 4883–4940,
1244 <https://doi.org/10.1021/cr020657y>, 2003.
- 1245 Vicars, W. C. and Savarino, J.: Quantitative constraints on the ^{17}O -excess ($\Delta^{17}\text{O}$) signature of surface ozone: Ambient
1246 measurements from 50°N to 50°S using the nitrite-coated filter technique, *Geochimica et Cosmochimica Acta*, 135, 270–
1247 287, <https://doi.org/10.1016/j.gca.2014.03.023>, 2014.
- 1248 Vicars, W. C., Bhattacharya, S. K., Erbland, J., and Savarino, J.: Measurement of the ^{17}O -excess ($\Delta^{17}\text{O}$) of tropospheric
1249 ozone using a nitrite-coated filter, *Rapid Communications in Mass Spectrometry*, 26, 1219–1231,
1250 <https://doi.org/10.1002/rcm.6218>, 2012.
- 1251 Vicars, W. C., Morin, S., Savarino, J., Wagner, N. L., Erbland, J., Vince, E., Martins, J. M. F., Lerner, B. M., Quinn, P. K.,
1252 Coffman, D. J., Williams, E. J., and Brown, S. S.: Spatial and diurnal variability in reactive nitrogen oxide chemistry as
1253 reflected in the isotopic composition of atmospheric nitrate: Results from the CalNex 2010 field study, *Journal of*
1254 *Geophysical Research: Atmospheres*, 118, 10,567-10,588, <https://doi.org/10.1002/jgrd.50680>, 2013.
- 1255 Vitousek, P. M., Aber, J. D., Howarth, R. W., Likens, G. E., Matson, P. A., Schindler, D. W., Schlesinger, W. H., and
1256 Tilman, D. G.: Human Alteration of the Global Nitrogen Cycle: Sources and Consequences, *Ecological Applications*, 7,
1257 737–750, [https://doi.org/10.1890/1051-0761\(1997\)007\[0737:HAOTGN\]2.0.CO;2](https://doi.org/10.1890/1051-0761(1997)007[0737:HAOTGN]2.0.CO;2), 1997.
- 1258 Walters, W. W. and Michalski, G.: Theoretical calculation of nitrogen isotope equilibrium exchange fractionation factors for
1259 various NO_y molecules, *Geochimica et Cosmochimica Acta*, 164, 284–297, <https://doi.org/10.1016/j.gca.2015.05.029>, 2015.
- 1260 Walters, W. W. and Michalski, G.: Theoretical calculation of oxygen equilibrium isotope fractionation factors involving
1261 various NO_y molecules, OH, and H_2O and its implications for isotope variations in atmospheric nitrate, *Geochimica et*
1262 *Cosmochimica Acta*, 191, 89–101, <https://doi.org/10.1016/j.gca.2016.06.039>, 2016.
- 1263 Walters, W. W., Tharp, B. D., Fang, H., Kozak, B. J., and Michalski, G.: Nitrogen isotope composition of thermally
1264 produced NO_x from various fossil-fuel combustion sources, *Environmental Science & Technology*, 49, 11363–11371,
1265 <https://doi.org/10.1021/acs.est.5b02769>, 2015a.
- 1266 Walters, W. W., Goodwin, S. R., and Michalski, G.: Nitrogen Stable Isotope Composition ($\delta^{15}\text{N}$) of Vehicle-Emitted NO_x ,
1267 *Environ. Sci. Technol.*, 49, 2278–2285, <https://doi.org/10.1021/es505580v>, 2015b.
- 1268 Walters, W. W., Simonini, D. S., and Michalski, G.: Nitrogen isotope exchange between NO and NO_2 and its implications
1269 for $\delta^{15}\text{N}$ variations in tropospheric NO_x and atmospheric nitrate, *Geophysical Research Letters*, 43, 440–448,
1270 <https://doi.org/10.1002/2015GL066438>, 2016.
- 1271 Walters, W. W., Fang, H., and Michalski, G.: Summertime diurnal variations in the isotopic composition of atmospheric
1272 nitrogen dioxide at a small midwestern United States city, *Atmospheric Environment*, 179, 1–11,
1273 <https://doi.org/10.1016/j.atmosenv.2018.01.047>, 2018.

- 1274 Wang, X., Jacob, D. J., Eastham, S. D., Sulprizio, M. P., Zhu, L., Chen, Q., Alexander, B., Sherwen, T., Evans, M. J., Lee,
1275 B. H., Haskins, J. D., Lopez-Hilfiker, F. D., Thornton, J. A., Huey, G. L., and Liao, H.: The role of chlorine in global
1276 tropospheric chemistry, *Atmospheric Chemistry and Physics*, 19, 3981–4003, <https://doi.org/10.5194/acp-19-3981-2019>,
1277 2019a.
- 1278 Wang, Y., Zhang, Q. Q., He, K., Zhang, Q., and Chai, L.: Sulfate-nitrate-ammonium aerosols over China: response to 2000–
1279 2015 emission changes of sulfur dioxide, nitrogen oxides, and ammonia, *Atmospheric Chemistry and Physics*, 13, 2635–
1280 2652, <https://doi.org/10.5194/acp-13-2635-2013>, 2013.
- 1281 Wang, Y., Gao, W., Wang, S., Song, T., Gong, Z., Ji, D., Wang, L., Liu, Z., Tang, G., Huo, Y., Tian, S., Li, J., Li, M., Yang,
1282 Y., Chu, B., Petäjä, T., Kerminen, V.-M., He, H., Hao, J., Kulmala, M., Wang, Y., and Zhang, Y.: Contrasting trends of
1283 PM_{2.5} and surface-ozone concentrations in China from 2013 to 2017, *National Science Review*, 7, 1331–1339,
1284 <https://doi.org/10.1093/nsr/nwaa032>, 2020.
- 1285 Wang, Y., Liu, J., Jiang, F., Chen, Z., Wu, L., Zhou, S., Pei, C., Kuang, Y., Cao, F., Zhang, Y., Fan, M., Zheng, J., Li, J., and
1286 Zhang, G.: Vertical measurements of stable nitrogen and oxygen isotope composition of fine particulate nitrate aerosol in
1287 Guangzhou city: Source apportionment and oxidation pathway, *Science of The Total Environment*, 865, 161239,
1288 <https://doi.org/10.1016/j.scitotenv.2022.161239>, 2023.
- 1289 Wang, Y. L., Song, W., Yang, W., Sun, X. C., Tong, Y. D., Wang, X. M., Liu, C. Q., Bai, Z. P., and Liu, Z. Y.: Influences of
1290 Atmospheric Pollution on the Contributions of Major Oxidation Pathways to PM_{2.5} Nitrate Formation in Beijing, *Journal of*
1291 *Geophysical Research: Atmospheres*, 124, 4174–4185, <https://doi.org/10.1029/2019JD030284>, 2019b.
- 1292 Wayne, R. P., Barnes, I., Biggs, P., Burrows, J. P., Canosa-Mas, C. E., Hjorth, J., Le Bras, G., Moortgat, G. K., Perner, D.,
1293 Poulet, G., Restelli, G., and Sidebottom, H.: The nitrate radical: Physics, chemistry, and the atmosphere, *Atmospheric*
1294 *Environment. Part A. General Topics*, 25, 1–203, [https://doi.org/10.1016/0960-1686\(91\)90192-A](https://doi.org/10.1016/0960-1686(91)90192-A), 1991.
- 1295 Weber, S., Uzu, G., Calas, A., Chevrier, F., Besombes, J.-L., Charron, A., Salameh, D., Ježek, I., Močnik, G., and Jaffrezo,
1296 J.-L.: An apportionment method for the oxidative potential of atmospheric particulate matter sources: application to a one-
1297 year study in Chamonix, France, *Atmospheric Chemistry and Physics*, 18, 9617–9629, [https://doi.org/10.5194/acp-18-9617-](https://doi.org/10.5194/acp-18-9617-2018)
1298 2018, 2018.
- 1299 Whiteman, C. D.: Breakup of Temperature Inversions in Deep Mountain Valleys: Part I. Observations, *Journal of Applied*
1300 *Meteorology and Climatology*, 21, 270–289, [https://doi.org/10.1175/1520-0450\(1982\)021<0270:BOTIID>2.0.CO;2](https://doi.org/10.1175/1520-0450(1982)021<0270:BOTIID>2.0.CO;2), 1982.
- 1301 WHO: World Health Organization global air quality guidelines: particulate matter (PM_{2.5} and PM₁₀), ozone, nitrogen
1302 dioxide, sulfur dioxide and carbon monoxide, 2021.
- 1303 Wild, O., Zhu, X., and Prather, M. J.: Fast-J: Accurate simulation of in- and below-cloud photolysis in tropospheric chemical
1304 models, *Journal of Atmospheric Chemistry*, 37, 245–282, <https://doi.org/10.1023/A:1006415919030>, 2000.
- 1305 Xue, C.: Substantially Growing Interest in the Chemistry of Nitrous Acid (HONO) in China: Current Achievements,
1306 Problems, and Future Directions, *Environ. Sci. Technol.*, 56, 7375–7377, <https://doi.org/10.1021/acs.est.2c02237>, 2022.
- 1307 Young, E. D., Galy, A., and Nagahara, H.: Kinetic and equilibrium mass-dependent isotope fractionation laws in nature and
1308 their geochemical and cosmochemical significance, *Geochimica et Cosmochimica Acta*, 66, 1095–1104,
1309 [https://doi.org/10.1016/S0016-7037\(01\)00832-8](https://doi.org/10.1016/S0016-7037(01)00832-8), 2002.
- 1310 Yu, Z. and Elliott, E. M.: Novel Method for Nitrogen Isotopic Analysis of Soil-Emitted Nitric Oxide, *Environ. Sci. Technol.*,
1311 51, 6268–6278, <https://doi.org/10.1021/acs.est.7b00592>, 2017.

- 1312 Zhang, L., Vet, R., O'Brien, J. M., Mihele, C., Liang, Z., and Wiebe, A.: Dry deposition of individual nitrogen species at
1313 eight Canadian rural sites, *Journal of Geophysical Research: Atmospheres*, 114, <https://doi.org/10.1029/2008JD010640>,
1314 2009.
- 1315 Zhang, R., Wang, G., Guo, S., Zamora, M. L., Ying, Q., Lin, Y., Wang, W., Hu, M., and Wang, Y.: Formation of Urban Fine
1316 Particulate Matter, *Chem. Rev.*, 115, 3803–3855, <https://doi.org/10.1021/acs.chemrev.5b00067>, 2015.
- 1317 Zhang, W., Bi, X., Zhang, Y., Wu, J., and Feng, Y.: Diesel vehicle emission accounts for the dominate NO_x source to
1318 atmospheric particulate nitrate in a coastal city: Insights from nitrate dual isotopes of PM_{2.5}, *Atmospheric Research*, 278,
1319 106328, <https://doi.org/10.1016/j.atmosres.2022.106328>, 2022a.
- 1320 Zhang, Y.-L., Zhang, W., Fan, M.-Y., Li, J., Fang, H., Cao, F., Lin, Y.-C., Wilkins, B. P., Liu, X., Bao, M., Hong, Y., and
1321 Michalski, G.: A diurnal story of $\Delta^{17}\text{O}(\text{NO}_3^-)$ in urban Nanjing and its implication for nitrate aerosol formation, *npj Clim
1322 Atmos Sci*, 5, 1–10, <https://doi.org/10.1038/s41612-022-00273-3>, 2022b.
- 1323 Zhou, W., Gao, M., He, Y., Wang, Q., Xie, C., Xu, W., Zhao, J., Du, W., Qiu, Y., Lei, L., Fu, P., Wang, Z., Worsnop, D. R.,
1324 Zhang, Q., and Sun, Y.: Response of aerosol chemistry to clean air action in Beijing, China: Insights from two-year ACSM
1325 measurements and model simulations, *Environmental Pollution*, 255, 113345, <https://doi.org/10.1016/j.envpol.2019.113345>,
1326 2019.
- 1327 Zong, Z., Wang, X., Tian, C., Chen, Y., Fang, Y., Zhang, F., Li, C., Sun, J., Li, J., and Zhang, G.: First Assessment of NO_x
1328 Sources at a Regional Background Site in North China Using Isotopic Analysis Linked with Modeling, *Environmental
1329 Science and Technology*, 51, 5923–5931, <https://doi.org/10.1021/acs.est.6b06316>, 2017.
- 1330 Zong, Z., Sun, Z., Xiao, L., Tian, C., Liu, J., Sha, Q., Li, J., Fang, Y., Zheng, J., and Zhang, G.: Insight into the Variability of
1331 the Nitrogen Isotope Composition of Vehicular NO_x in China, *Environ. Sci. Technol.*, [acs.est.0c04749](https://doi.org/10.1021/acs.est.0c04749),
1332 <https://doi.org/10.1021/acs.est.0c04749>, 2020.

1333